Comprehensive global dataset of uniformly processed shear-wave splitting measurements

Jonathan Wolf[1,2⋆], Thorsten W. Becker[3,4,5], Edward Garnero[6], Kelly H. Liu[7], John D. West[6]

[1] *Department of Earth and Planetary Science, University of California, Berkeley, CA, USA*
[2] *Miller Institute for Basic Research in Science, Berkeley, CA, USA*
[3] *Institute for Geophysics, Jackson School of Geosciences, The University of Texas at Austin, TX, USA*
[4] *Department of Earth and Planetary Sciences, Jackson School of Geosciences, The University of Texas at Austin, TX, USA*
[5] *Oden Institute for Computational Engineering & Sciences, The University of Texas at Austin, TX, USA*
[6] *School of Earth and Space Exploration, Arizona State University, Tempe, AZ, USA*
[7] *Department of Earth Sciences and Engineering, Missouri University of Science and Technology, Rolla, MO, USA*

February 13, 2025

SUMMARY

Seismic anisotropy can inform us about convective flow in the mantle. Shear waves traveling through azimuthally anisotropic regions split into fast and slow pulses, and measuring the resulting shear-wave splitting provides some of the most direct insights into Earth's interior dynamics. Shear-wave splitting is a constraint for path-averaged azimuthal anisotropy and is often studied regionally. Global compilations of these measurements also exist. Such compilations include measurements obtained using different data processing methodologies (e.g., filtering), which do not necessarily yield identical results, and reproducing a number of studies can be challenging given that not all provide the required information, e.g., about the source location. Here, we automatically determine SKS, SKKS and PKS shear-wave splitting parameters from a global dataset. This dataset includes all earthquakes with magnitudes ≥ 5.9 from 2000 to the present, collected from 24 data centers, totaling over 4,700 events and 16 million three-component seismograms. We obtain approximately 90,000 robust measurements for "fast azimuth", ϕ, and delay time, δt, and 210,000 robust null measurements. Results generally agree with previous work but our measurements allow us to identify hundreds of "null stations" below which the mantle appears effectively isotropic with respect to azimuthal anisotropy, which are important for some splitting techniques. We make all measurements publicly available as a data product, along with detailed metadata. This serves two purposes: ensuring full reproducibility of results and providing all necessary information for future systematic use of our measurements, in tomography applications or comparisons with geodynamic flow predictions.

Key words: Shear-wave splitting – Global compilation – Seismic anisotropy – Mantle flow.

1 INTRODUCTION

Seismic anisotropy refers to the phenomenon by which seismic waves travel at different velocities depending on their propagation direction and/or polarization. In the mantle, anisotropy arises due to two primary mechanisms which can both be linked to Earth's internal deformation and convective evolution: (1) Crystallographic-preferred orientation (CPO), where intrinsically anisotropic mineral crystals align under finite deformation with their directional elastic properties, and (2) shape-preferred

⋆ jonathan.wolf@berkeley.edu

orientation (SPO), involving aligned isotropic or anisotropic materials, e.g., layered composites, that can be effectively anisotropic on the scales seen by the dominant seismic wavelength (e.g., Nicolas and Christensen, 1987; Silver, 1996; Kocks et al., 2000; Long and Becker, 2010; Romanowicz and Wenk, 2017). The detection and characterization of seismic anisotropy can provide valuable information on convective flow in Earth's mantle (e.g., Tanimoto and Anderson, 1984; Gaboret et al., 2003; Becker et al., 2003; Nowacki et al., 2011; Wolf et al., 2024a). For the typical, "A" type CPOs of olivine, as they might form under dislocation creep in the upper mantle, the fast propagation direction of upper mantle anisotropy is expected to align with shear in mantle flow. Different alignments might be caused by high volatile and/or stress type CPO formation (e.g., Kneller et al., 2005; Lassak et al., 2006; Becker et al., 2008), although those fabrics appear less common and less systematic in the rock record (e.g., Bernard et al., 2019). However, in the deepest mantle, the relationship between anisotropy and flow is more complicated (e.g., Yamazaki and Karato, 2001; Wookey and Kendall, 2008; Creasy et al., 2020); it cannot necessarily be assumed the polarization direction of the fast traveling wave corresponds to the direction of convective flow (e.g., Yamazaki and Karato, 2001; Nowacki et al., 2011; Wolf and Long, 2022). Seismic anisotropy is usually stronger in the upper than in the lowermost mantle (e.g., Romanowicz and Wenk, 2017; Becker and Lebedev, 2021). Therefore, fast directions of shear wave splitting measurements are routinely interpreted as being due to upper mantle flow (e.g., Silver, 1996; Fouch et al., 2000; Behn et al., 2004; Becker et al., 2006).

The SKS, SKKS and PKS (Figure 1a) seismic phases, hereafter referred to as *KS, are SV polarized upon reentry into the mantle from the outer core. If a *KS wave travels through an anisotropic region in the receiver-side mantle, it splits into two pulses, one of which travels faster than the other. This phenomenon can occur in Earth's upper mantle, as schematically shown in Figure 1b. The two components (red and blue in Figure 1b) accumulate a time lag, or relative delay time, δt, which increases as a function of the distance traveled through the anisotropic material. We denote the polarization orientation of the fast pulse, or "fast axis", as ϕ (counted clockwise from the North; Figure 1c). These two parameters characterize seismic anisotropy for a typical shear wave splitting measurement (Ando et al., 1983; Vinnik et al., 1984; Silver and Chan, 1991).

Shear wave splitting parameters $\{\phi, \delta t\}$ are typically determined through manual or semi-automated inspection and analysis of data (e.g., Teanby et al., 2004; Wüstefeld et al., 2010, 2008; Reiss and Rümpker, 2017), although fully automated approaches have also been applied (e.g., Evans et al., 2006; Liu et al., 2014; Walpole et al., 2014; Link et al., 2022; Hudson et al., 2023). Results from these manual analyses as well as those derived from automatic approaches have been compiled into large splitting parameter collections (e.g., Silver, 1996; Wüstefeld et al., 2009). These compilations have provided valuable insights into upper mantle flow and have enabled detailed comparisons between shear-wave splitting (from *KS body waves) and surface wave wave inversions (e.g., Montagner et al., 2000; Wüstefeld et al., 2009; Becker et al., 2012). However, global compilations include splitting parameters from studies that use different data processing techniques, which can vary depending on the periods used in analyses and the methods employed to calculate splitting parameters (Savage, 1999; Long and van der Hilst, 2005; Vecsey et al., 2008; Kong et al., 2015). Additionally, some studies do not provide specific information on the earthquake data used to determine splitting parameters, making it challenging (if not impossible) to reproduce their results, or

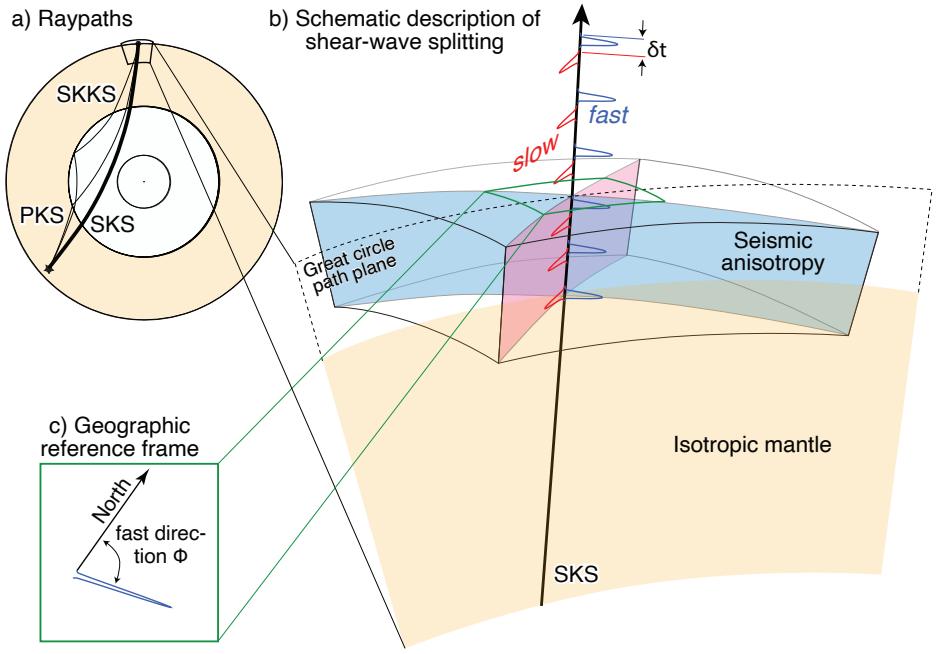

Figure 1. Schematic representation of shear-wave splitting due to upper mantle anisotropy. a) Schematic Earth cross-section showing PKS, SKS and SKKS (*KS) raypaths. (b) In presence of seismic anisotropy in the upper mantle, *KS splits into fast (blue) and slow (red) traveling components with mutually orthogonal polarizations. These components accumulate a relative time lag (δt); additionally, the fast polarization direction can be measured. (c) Fast polarization direction ϕ relative to geographic north.

to analyze features such as backazimuthal dependence of ϕ and δt which can provide insights into the nature of anisotropy at depth (e.g., Silver and Savage, 1994; Rümpker and Silver, 1998; Chevrot and van der Hilst, 2003).

Here we automatically measure shear-wave splitting for all earthquakes with magnitudes $\geq$ 5.9 from the year 2000 to present, which were collected from 24 data centers worldwide. We obtain approximately 90,000 well-constrained sets of $\{\phi, \delta t\}$ pairs and 210,000 null measurements. This automatic measurement database is substantially larger than previous ones (e.g., Liu et al., 2014; Walpole et al., 2014). The measurements are compared to existing databases and previous automatic splitting efforts and found generally consistent with previous results. We identify hundreds of stations worldwide at which a large majority of *KS waves is unsplit, which are called null stations. Null measurements, at which waves appear not influenced by azimuthal seismic anisotropy in the mantle, provide important information (e.g., Wüstefeld and Bokelmann, 2007; Walpole et al., 2014). Effective "null stations" are essential for the application of some splitting strategies, such as determining S-wave source-side anisotropy (e.g., Russo and Silver, 1994; Foley and Long, 2011; Lynner and Long, 2013), PS bounce point anisotropy (e.g., Wolf et al., 2024c), and inferring lowermost mantle anisotropy from ScS and S_{diff} waves (e.g., Wolf and Long, 2024; Wolf et al., 2022).

The code we use to measure shear-wave splitting is publicly available, and we publish our uniformly processed measurements as well as metadata. This enables reproducibility and the extraction of information such as backazimuthal dependence of splitting parameters. We anticipate that this work will enable new inquiries into Earth's dynamic interior processes using uniformly made measurements from a large global dataset.

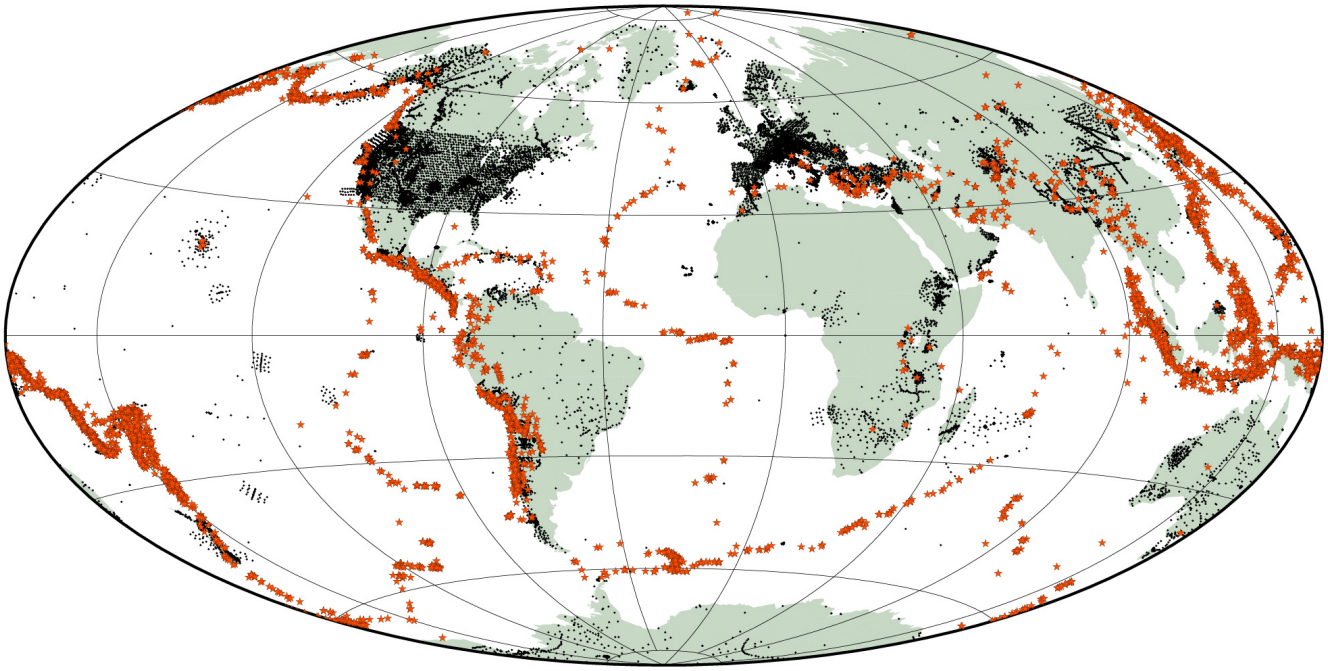

Figure 2. Source-receiver configuration used in this study. Stations are shown as black circles and events as orange stars. We use data from approximately 4,700 different events and 25,000 distinct stations.

2 DATASET AND PRE-PROCESSING

We have collected (and continue collecting) all available data from 24 global data centers from January 1, 2000, to present, for all seismic events with moment magnitudes 5.9 and above (hereafter referred to as the ADEPT dataset, `http://adept.sese.asu.edu/`). We collect 2 hours of data for all stations, instrument deconvolve the data to displacement, rotate the horizontal components to radial and transverse motions, and downsample the seismograms to 20 samples per second. We store the data locally in event-based directories. To date, we have collected over 4700 earthquakes (and over 16 million three-component earthquake recordings). All events and stations that are included in the dataset are shown in Figure 2. The corresponding ~ 500 seismic networks and their citations are provided in the Supplementary Material.

3 SHEAR-WAVE SPLITTING MEASUREMENTS

We conduct shear-wave splitting measurements using the SplitRacerAUTO MATLAB code (Reiss and Rümpker, 2017; Link et al., 2022). SplitRacerAUTO uses the transverse energy minimization technique (Silver and Chan, 1991) with the uncertainty quantification by Walsh et al. (2013) to determine ϕ and δt. This is repeated for a certain number (we choose 30) of randomly selected time intervals around the expected phase arrival, and measurements are only used if they are robust across all time windows. The details of this procedure are described in the original publication by Reiss and Rümpker (2017). SplitRacerAUTO additionally calculates the splitting intensity SI (Chevrot, 2000), which can be expressed as $SI \approx \delta t \sin(2(\alpha - \phi))$, where α is the backazimuth for *KS phases.

The first step of SplitRacerAUTO is to conduct data preprocessing all selected data. We use PKS waves measured at

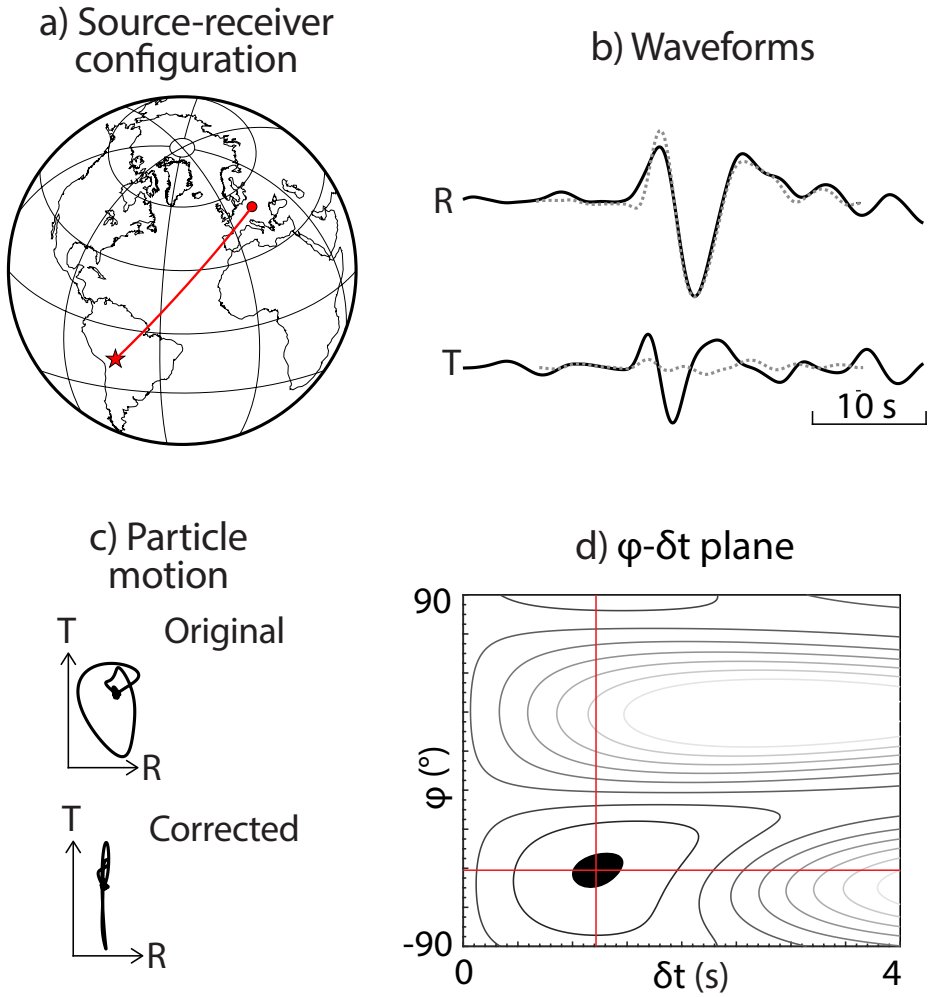

Figure 3. Example of a shear-wave splitting measurement. (a) Event (red star) that occurred on November 22, 2011, beneath central Bolivia and station OJC (red circle) located in Poland. The great-circle path is shown as a red line. (b) Radial (R) and transverse (T) component displacement waveforms. Waveforms corrected for the best-fitting splitting parameters are shown as gray dotted lines. (c) Particle motions (radial vs. transverse amplitude) for the original waveform (top) after after correction for the best-fitting splitting parameters (bottom). (d) Best-fitting splitting parameters in the ϕ-δt-plane. Black region indicates 95% confidence interval. The best-fitting ϕ and δt values are indicated by a red line. Contour lines show different transverse energy component levels.

epicentral distances from their inception and $< 155°$, SKS at distances $> 85°$ to their maximum distance, and SKKS at distances $> 100°$ to their maximum distance. In the preprocessing, SplitRacerAUTO discards data with low signal-to-noise ratios (SNRs). SNRs are calculated using an effective horizontal component ($\sqrt{R(t)^2 + T(t)^2}$, R(t)=radial component, T(t)=transverse component), and comparing the mean amplitude of a noise window with the signal window. The noise window is 20 s long and ends 5 s prior to the PREM-predicted arrival time. We set an SNR threshold of 2.2 after applying a butterworth bandpass filter of order 2 to retain periods between 6 and 25 s. Next, SplitRacerAUTO uses an additional quality-control algorithm to identify the time window in which the *KS phase under study arrives, avoiding *KS phases that coincide S, ScS and S_{diff} arrivals. In the third step, shear-wave splitting parameters are calculated, and measurements are automatically classified. For more details about SplitRacerAUTO, we refer to Link et al. (2022), which includes a thorough benchmark against measurements for which time windows were manually selected and measurements visually classified.

Several modifications have been made to the original code to tailor it for our purposes. We adjust SplitRacerAUTO to read

data from event-based directories instead of station-based ones. This data is already rotated into a radial-transverse coordinate frame based on station metadata. To enhance computational speed, which is essential given the large number of seismograms used in this study, we downsample all data to 3 samples per second instead of 20 (that SplitRacerAUTO uses per default). We also found that null measurements can be reliably identified using a single time window. Therefore, if a splitting measurement is null, we do not analyze additional time windows. The same applies if the splitting in the first time window is classified as clearly poor. Although these adjustments are minor and do not impact SplitRacerAUTO's core functionality, they increase computational speeds by a factor of about 200. Our slightly adjusted SplitRacerAUTO version can be found at `https://doi.org/10.5281/zenodo.14834413` (Wolf et al., 2025).

Figure 3 illustrates an example of an SKS shear-wave splitting measurement from data collected at station OJC in Poland, for an event that occurred on November 22, 2011 beneath central Bolivia. In this example, the SKS signal is clearly above the noise level (Figure 3b), the original particle motion is elliptical, and after correcting for the best-fitting splitting parameters, the particle motion becomes linear (Figure 3c). The best-fitting $\{\phi, \delta t\}$ (Figure 3d) splitting parameters are tightly constrained.

SplitRacerAUTO assigns several categories to measurements: good, average, null, and poor. The criteria used for these categorizations are detailed by Link et al. (2022), and we apply the same criteria in this study to assign 'good' and 'average' labels to our *KS splitting measurements. These criteria include maximum permissible error bars on δt, minimum required energy reductions for the corrected traces and minimum permissible eigenvalue ratios of the calculated covariance matrix. However, we define null measurements less strictly than Link et al. (2022): we label measurements as 'null' if $|SI| < 0.3$ (instead of < 0.15) and the ratio of the first and second eigenvalues of the covariance matrix is < 0.1 (instead of < 0.06). The decision on how narrowly to define a null measurement is somewhat arbitrary; we adopt this broader SI range for a null definition for practical reasons. Measurements with $|SI| < 0.3$ do not yield well-constrained $\{\phi, \delta t\}$ values because the splitting is too weak (at the periods we are using). Defining these measurements as null allows us to measure splitting for only one time window, thereby not unnecessarily straining our computational resources. In practice, this definition of null measurements has no influence on the determination of null stations, which are often defined by a percentage of unsplit waves measured at them (e.g., Walpole et al., 2014). In this study, we set a higher threshold for the percentage of nulls required to define null stations compared to previous studies. This approach explicitly accounts for weakly split waves that meet our quality criteria but would likely have been discarded as poor in previous studies.

4 RESULTS

4.1 Global splitting measurements

We obtain $64{,}154$ SKS, $14{,}439$ SKKS, and $8{,}153$ PKS global $\{\phi, \delta t\}$ measurements. These results are presented in Figure 4 in a global overview, and Figure 5 for regional example zoom-ins.

The overall measurement coverage is largely determined by the station distribution (Figure 2), and consequently, the availability of publicly accessible seismic data that is part of ADEPT. For example, the measurement density is very high in

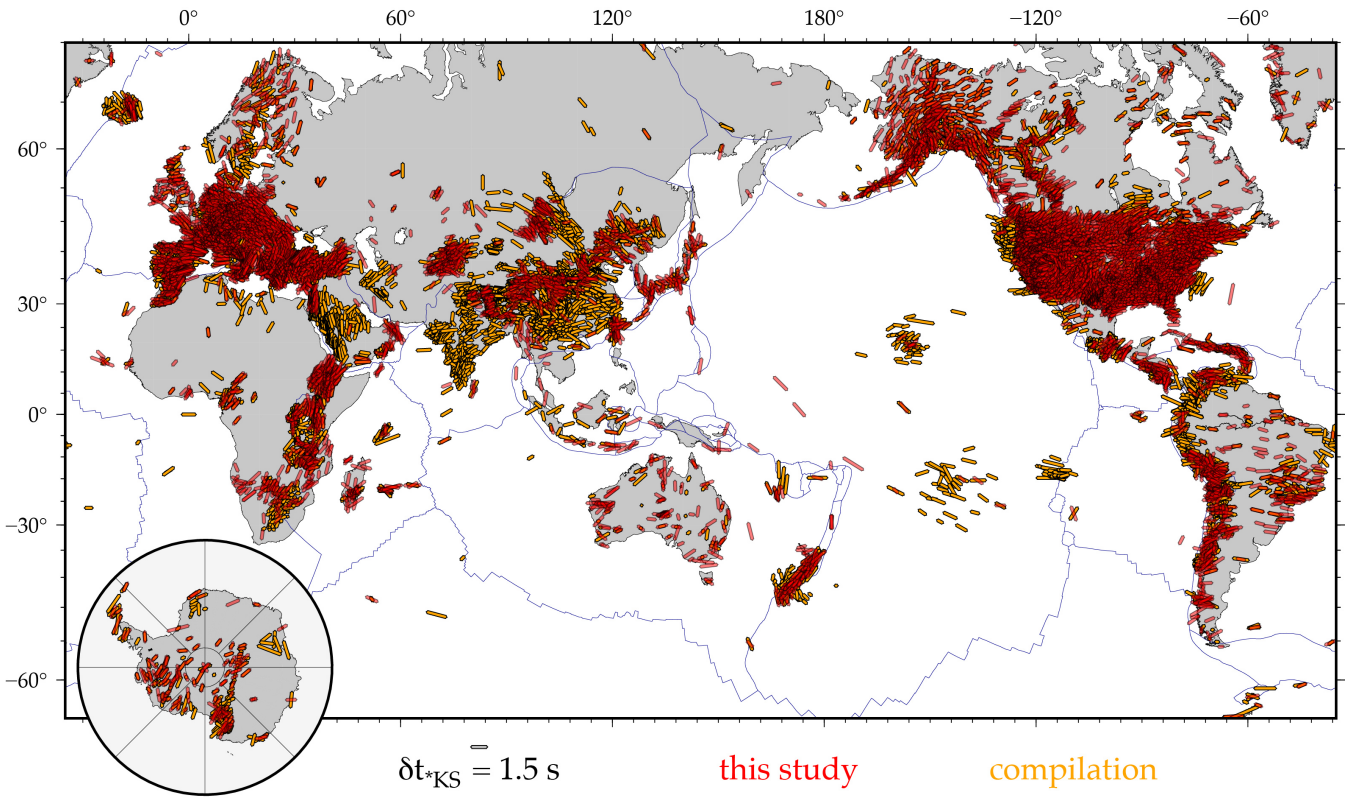

Figure 4. Comparison of global splitting coverage and fast directions between this study (red sticks) and the updated compilation from Becker et al. (2012) (orange sticks, including the Montpellier database of Wüstefeld et al. (2009) with last updates from 2020), with plate boundaries from Bird (2003) in blue. Results for Antarctica are shown as an inset; see Figure 5 and Figure 7 for regional zoom ins. The compilation includes results from restricted data in China, India and Saudi Arabia, leading to better coverage in these regions. Our study adds more coverage in northern Europe, Australia, southern Africa, central Asia and a stretch of Chile.

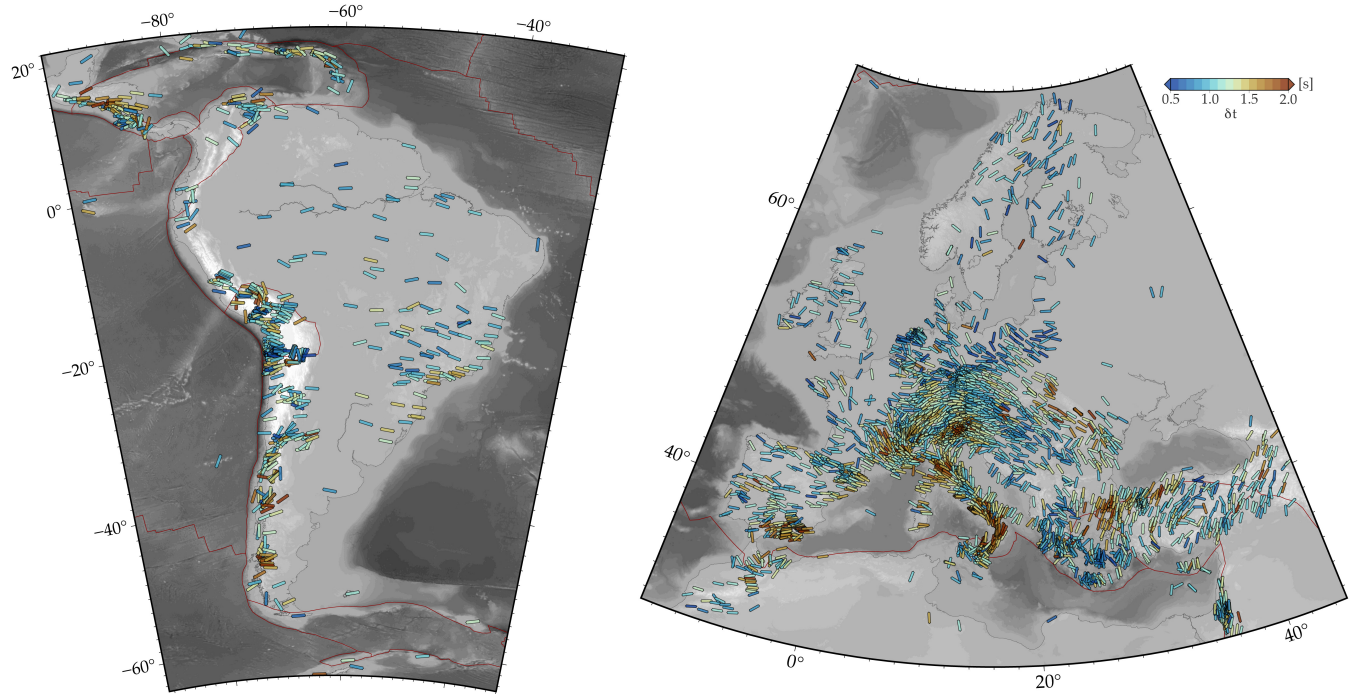

Figure 5. Regional $\{\phi, \delta t\}$ measurement results from our automated analysis for South America (left) and Europe (right). Colored sticks are centered at the station at which splitting was measured. Their orientation indicates the polarization direction ϕ and the color scale represents the delay time δt (legend). Plate boundaries from Bird (2003).

the United States and Europe, while significantly fewer measurements are available for stations in Russia and India. Outside of Europe and North America, countries such as Chile, Japan, Taiwan, New Zealand, Tajikistan, and Kyrgyzstan are particularly well sampled.

4.2 Null measurements

In addition to the splitting parameters $\{\phi, \delta t\}$, we identify which measurements are unsplit or null. Stations where a large majority of records show no splitting are often referred to as null stations, yet this is important information, as noted above. We introduce two distinct categories of null stations. If at least 97.5 % of the records at a station are unsplit, and the station is sampled from more than one 30°-wide azimuth, the station is assigned a null category label A. If between 95.0 % and 97.5 % of the measurements are null, the station is classified as category B. For a station to be included in either of these categories, it must have more than 30 null or $\{\phi, \delta t\}$ measurements. Figure 6 shows null stations as colored circles for category A and as gray circles for category B. The color of the circle indicates how many 30° backazimuthal bins (starting at backazimuth = 0°) contain measurements. In total, we identify 178 category A and 371 category B null stations, many of which are located in the United States and Europe (Figure 6b,c).

4.3 Data product description

We make the global $\{\phi, \delta t\}$ and null measurements publicly available. For each phase (SKS, SKKS, PKS), we provide a .txt file that includes the following information: event name, for example '200001081647', corresponding to an event that occurred on January 8, 2000 at 4:47pm UTC; event latitude (°); event longitude (°); event depth (km); station name; network name; station latitude (°); station longitude (°); quality tag; δt (s); δt upper error bound (s); δt lower error bound (s); ϕ (°); ϕ upper error bound (°); ϕ lower error bound (°); splitting intensity; splitting intensity upper error bound; splitting intensity lower error bound. These measurements are also available on the data product website associated with this large data collection effort, `http://swat.sese.asu.edu`. Measurements will occasionally be updated on the website as the ADEPT dataset continues to grow.

For each $\{\phi, \delta t\}$ and null measurement used in this study, we provide diagnostic splitting plots at `http://swat.sese.asu.edu`. These graphics, minimally edited from SplitRacerAUTO, include the waveforms, particle motions, ϕ-δt energy maps (similar to Figure 3b-d) and histograms that show the robustness of the splitting measurements across multiple time windows. These graphical products enable researchers to visually evaluate each splitting measurement for their own use.

Additionally, we include .txt files in the Supplementary Information with both category A and B null measurements. The format of these files is: station name, event name, number of robust measurements at the station, station latitude (°), station longitude (°).

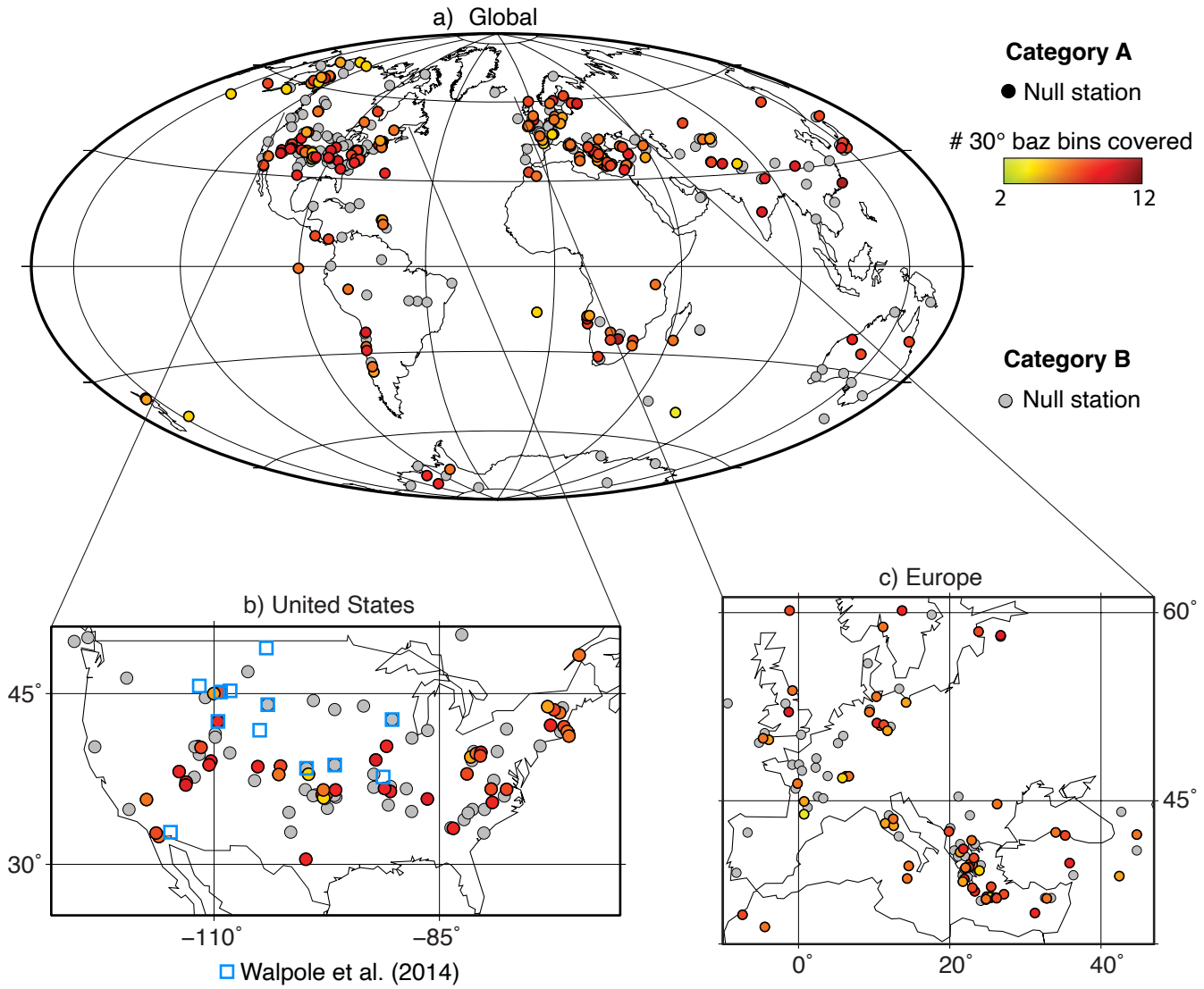

Figure 6. Null stations identified in this study. Category A null stations (stations where $> 97.5\%$ of measurements are null, which show sampling from 2 or more 30° backazimuthal bins) are represented as colored circles, the color scale legend indicates the number of 30° backazimuthal bins from which measurements were obtained. Category B null stations (stations having between 95% and 97.5% null measurements) are displayed as gray circles. (a) All null stations. (b) Zoom-in centered on the United States with null stations from Walpole et al. (2014) shown as blue squares. (c) Zoom-in centered on Europe.

5 COMPARISONS TO PREVIOUS STUDIES

5.1 Fast directions and delay times across the continental United States

We focus on the continental United States and its surrounding regions to compare our results with those of previous studies. This region is chosen for its exceptionally dense station coverage, primarily due to the prior deployment of USArray (IRIS Transportable Array, 2003), and because several automatic splitting approaches have been applied here (e.g., Walpole et al., 2014; Liu et al., 2014; Yang et al., 2017; Link et al., 2022). Specifically, we conduct a detailed comparison of our results with the updated composite compilation of manually picked splitting measurements by Becker et al. (2012) which includes the Montpellier database of Wüstefeld et al. (2009) with last updates from 2020, and the automatic measurements by Walpole

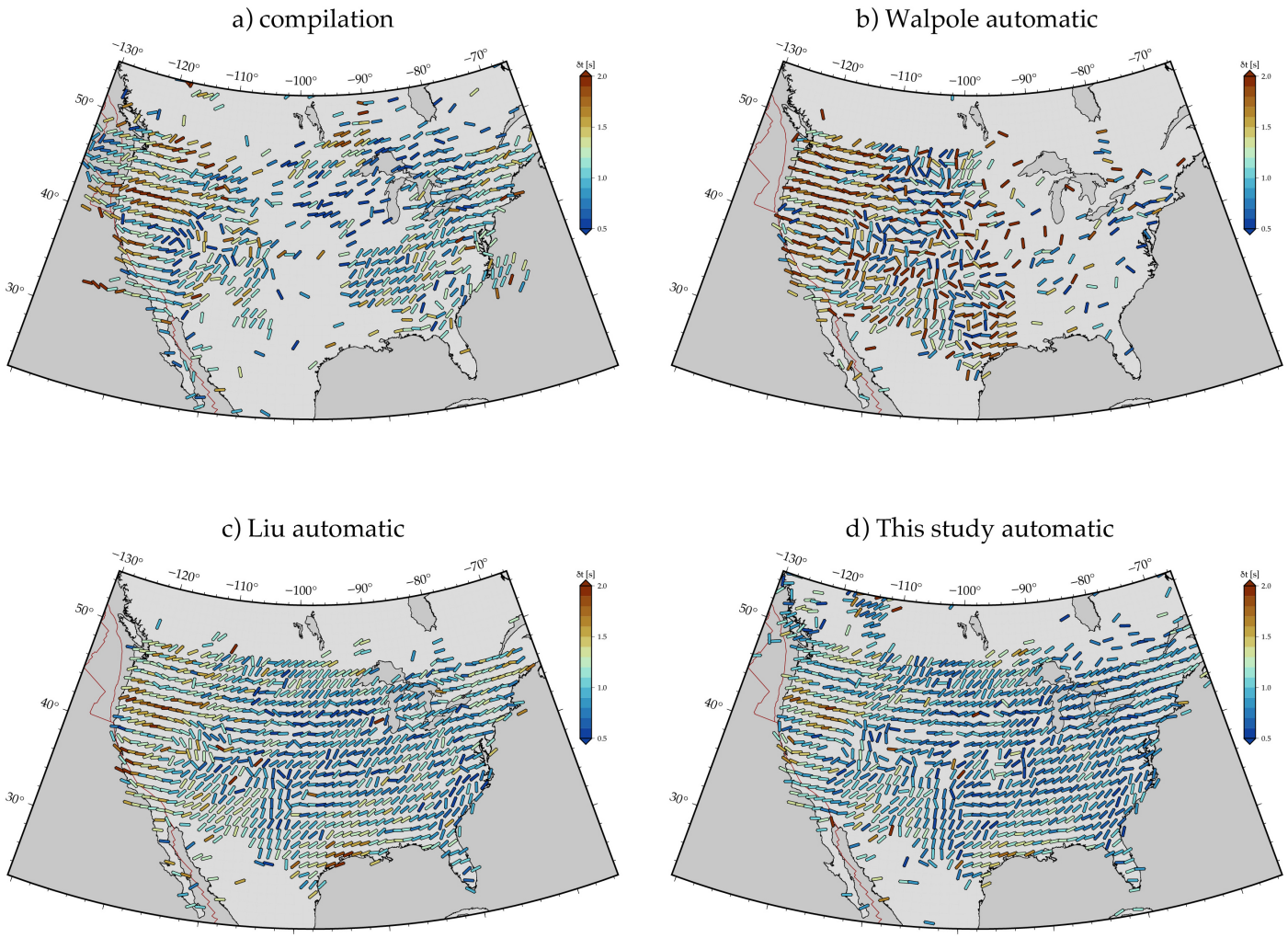

Figure 7. Averaged ($1^\circ \times 1^\circ$ bins) shear-wave splitting parameters across the continental United States and the surrounding regions. Results are shown for (a) the updated compilation of manually measured splitting parameters from Becker et al. (2012) which includes the Montpellier database of Wüstefeld et al. (2009) with last updates from 2020, (b) results from the global automated analysis by Walpole et al. (2014), (c) the automatic USArray results from Liu et al. (2014) and Yang et al. (2017), and, (d) this study. Colored sticks are centered at the station at which splitting was measured. Their orientation indicates the polarization direction ϕ and the color scale represents the delay time δt (legend).

et al. (2014) who provided a global database, as well as automated splits from Liu et al. (2014) and Yang et al. (2017) which are restricted to North America/USArray.

For comparative analysis, we first calculate the station average and then spatially average these splits, but we note that backazimuthal information is retained in the original databases. All averaging is based on delay-time weighted, orientational (i.e., 180° periodic) vector means, and computing the median values within spatial bins. We show $1^\circ \times 1^\circ$ splitting averages for all four approaches in Figure 7. Results from all compilations or automated approaches display the same overall patterns, but details differ in certain regions. Our measurements (Figure 7d) generally most resemble those obtained by Liu-Yang (Figure 7c), whereas there are more differences to the compilation of manually picked measurements (Figure 7a), as might be expected, and the automated analysis of Walpole et al. (2014) (Figure 7b). The most significant differences from the manual splitting compilation are in the mid United States, where the compilation includes a relatively low number of measurements, whereas the agreement is better on both coasts. Both fast polarization directions and delay times from the manual splitting compilation

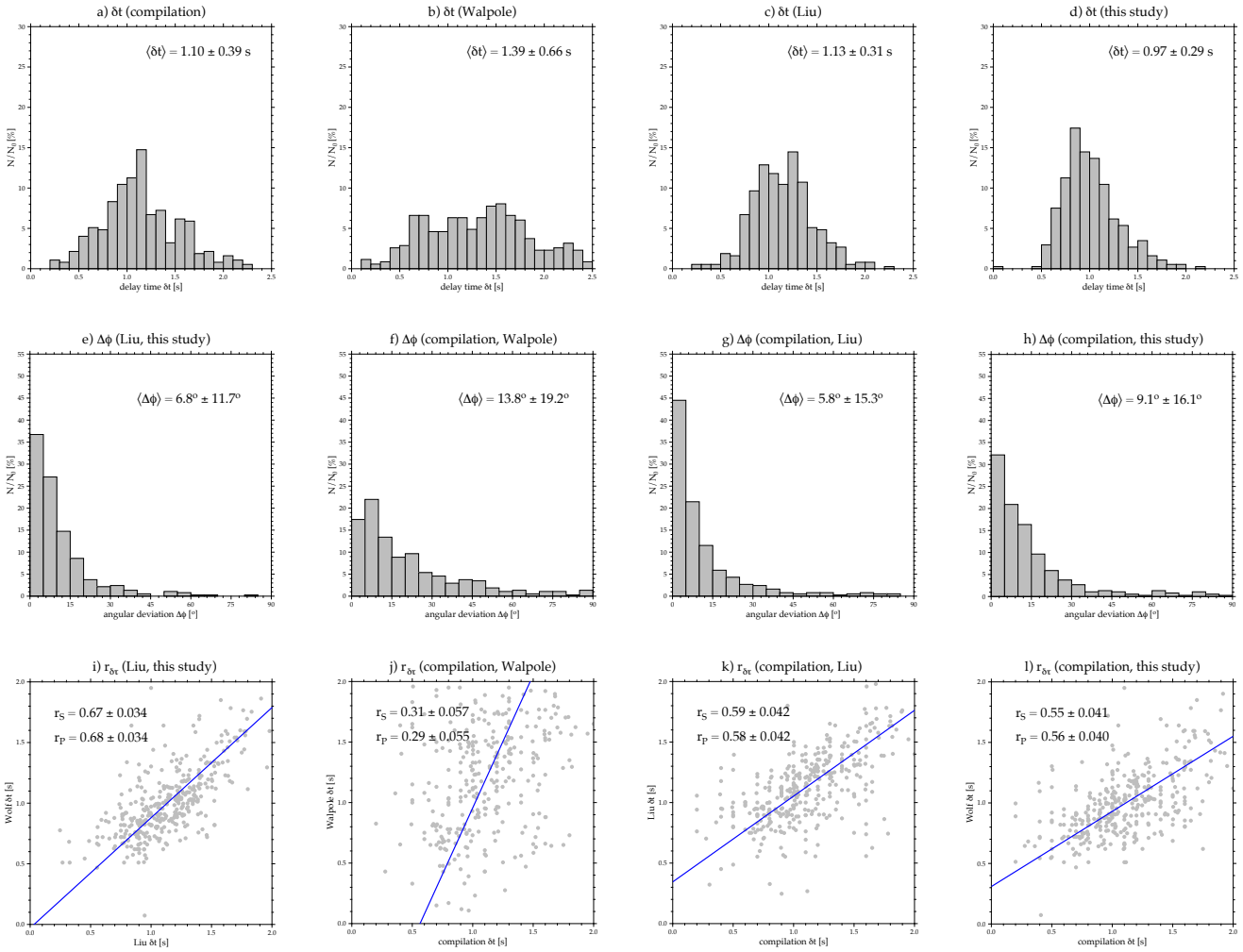

Figure 8. Statistical comparison of the binned splitting results shown in Figure 7 for North America for regions covered by the respective datasets. "Compilation" refers to the updated compilation of manual splitting studies from Becker et al. (2012), "Walpole" to the automated measurements of Walpole et al. (2014), and "Liu" to the automatic measurements from Liu et al. (2014) and Yang et al. (2017). (a-d) Distribution of δt values and mean values $\pm$ standard deviation for (a) the compilation of regional studies, and the automated results from (b) Walpole, (c) Liu, and (d) this study. (e-h) Fast polarization differences, $\Delta\phi$ and mean values between pairs of studies: (e) Liu-this study, (f) compilation-Walpole, (g) compilation-Liu, (h) compilation-this study. (i-l) Relationships between delay times δt between the same pairs of studies. The Pearson and Spearman rank correlations are provided as r_p and r_s with errors from bootstrapping. In general, our results are more similar to the previous automatic measurements of Liu than the compilation, but differences are larger compared to Walpole's automated estimates (not shown) which are also less similar to the compilation.

show less smooth patterns compared to the automation-based Wolf and Liu-Yang studies. The fast directions from the Walpole study roughly resemble the other approaches along the west coast of the United States, while agreement is less in the other areas.

We also conduct a statistical comparison between the measurements obtained in this study, the compilation of hand-picked measurements, and the previous Liu-Yang automated splitting measurement approach. The splitting compilation generally shows a broader spread of δt values than Liu and our study using automation-based measurements (Figure 8a, c, d), with Walpole's database showing an even wider spread (Figure 8b). The mean (expected) value of the delay time distribution are more similar for the compilation and Liu-Yang, with our estimates being $\sim 0.1 - 0.2$ s below those two for North America, and more scatter for Walpole's automated approach. Amplitude differences could potentially be explained by the broader variety of filters used to measure shear-wave splitting for these manually determined measurements. For example, for manual

measurements, higher frequencies (up to $\sim$0.5 Hz) can be used to measure δt for low splitting strength and lower frequencies (up to $\sim$0.1 Hz) for larger splitting strengths, whereas we consistently use a bandpass filter between 6 and 25 s (see Section 3). This ensures consistency and comparability among measurements, but may not be ideal for any splitting strength.

We also analyze the differences in ϕ (Figure 8e-h) and δt (Figure 8i-l) across the compilation and the three automated splitting approaches. As suspected based on Figure 7, the statistical comparison shows that the results from our study are most similar to the Liu's automatic measurement approach. For both ϕ and δt, our results show a slightly greater deviation from the splitting compilation than the previous Liu-Yang automatic approach, while Walpole's estimates show larger deviations, $\sim$ twice the mean $\Delta\phi$ deviations from the compilation. Focusing on the difference between our and Liu's approach which are more comparable, those remaining more subtle differences may arise from our choice of a 6 s lower period bound of our bandpass-filter, which is generally higher (in period) than most studies in which splitting measurements are manually determined. Liu et al. (2014) and Yang et al. (2017) use a lower value of 2 s.

In general, there are multiple potential reasons for the differences between this and the previous studies that used automatic processing compared to the manual splitting compilation. First, data pre-processing varies among studies contributing to the splitting compilation. For instance, different filtering techniques are used on seismic data, and shear-wave splitting can depend on frequency (e.g., Savage, 1999; Wüstefeld et al., 2008; Wirth and Long, 2010). Second, the methods for measuring splitting may differ from the automatic approaches, which both use the transverse energy minimization technique (Silver and Chan, 1991). Other methods include the rotation-correlation method (Bowman and Ando, 1987) and the multichannel method (Chevrot, 2000). These different methods do not always produce identical results (e.g., Savage, 1999; Long and van der Hilst, 2005; Vecsey et al., 2008). Third, some studies determine the incoming backazimuth from the long-axis of the particle motion ellipse at long periods and correct the rotation of the horizontal seismogram accordingly (e.g., Liu and Gao, 2013; Wolf and Long, 2023). Others (e.g., Ekström and Busby, 2008; Reiss et al., 2019) determine an average station misorientation and adjust the splitting measurements based on that, while again others (e.g., Wolfe and Solomon, 1998) rely solely on the station misorientation provided by the data agency. These approaches vary among studies contributing to the splitting compilation. In our study, we determine the incoming backazimuth from the long-period (8-50 s) particle motion and correct the seismogram for a maximum misorientation value of 5°. If the calculated misorientation exceeds this value, no splitting parameters are determined. A systematic comparison of our individual splitting measurements with those from the splitting compilation is not possible, as many previous studies compiled in the compilation do not specify results for individual events at each station.

The Liu-Yang automatic measurements include event information for individual results, which allows us to identify the station-event pairs shared between their studies and ours. Of the 4,000 shared station-event pairs, only 15 measurements from Liu-Yang fall outside our 95% confidence intervals for either ϕ or δt. To investigate these 15 pairs in detail, we repeat splitting measurements using the same data processing as described by Liu et al. (2014). Specifically, we apply a 2-25 s bandpass-filter and do not correct for the slight backazimuthal difference determined from the long-axis of the particle motion for the individual seismogram. By adopting this approach, we generally replicate results similar to those from Liu-Yang, though minor

differences remain that could be caused a slightly different time window selection. An example of this is shown in Figure S1 of the Supplementary Material.

5.2 Global coverage

Figure 4 compares our uniformly measured dataset to the 2024 updated measurement compilation of Becker et al. (2012) which includes the database of Wüstefeld et al. (2009) updated as of 2020. The Becker compilation contains splitting measurements from restricted data that we do not have access to, for example in India, China and Saudi Arabia. Therefore, the compilation has much denser coverage in these regions. Compared to the compilation, our measurements add coverage in the central United States, northern Europe, Tajikistan, Kyrgyzstan, Australia and South America. However, this does not necessarily imply that we are the first to measure shear-wave splitting in these regions. Moreover, some existing regional studies are not part of the Wüstefeld et al. (2009) or Becker et al. (2012) compilations.

Figure 9a compares a generalized spherical harmonics expansion (cf. Becker et al., 2007) of a combination of the compilation of Becker et al. (2012) and our new automated SKS measurements with surface wave based estimates of azimuthal and radial anisotropy at asthenospheric mantle depths (175 km). As has been discussed widely, patterns of seismic anisotropy in the upper mantle are broadly consistent with convective flow in boundary layers (e.g. Tanimoto and Anderson, 1984; Montagner, 1998; Becker et al., 2008) and SKS splitting fast axes match surface wave based azimuthal anisotropy patterns on the largest scales (Montagner et al., 2000; Wüstefeld et al., 2009; Becker et al., 2012) with remaining debate about the origin of regional deviations even on scales visible on Figure 9a.

Figure 9b shows a quantitative comparison in terms of global correlation up to spherical harmonic degree $\ell = 20$, r_{20}. In this update of a similar computation shown in Becker and Lebedev (2021), the match between smoothed SKS and surface wave estimates from SL2013SVA (Schaeffer and Lebedev, 2013) and YB13SV (Yuan and Beghein, 2013) is improved slightly in the upper ~ 300 km of the mantle where we expect CPO formation under dislocation creep to dominate. The comparison with 3D2018 (Debayle et al., 2016) shows a statistically significant negative correlation at ~ 350 km. This is consistent with the comparison of Becker and Lebedev (2021) with an earlier version of the 3D2018 class of models; the physical process causing such a mismatch remain are unclear, with vertical coherence of anisotropy patterns being one possible avenue for further refinement (Yuan and Beghein, 2013).

5.3 Null stations

We compare our identified null stations to the previous work of Lynner and Long (2013) and Walpole et al. (2014). The reason to use these two studies for comparison is that they used a uniform methodology to identify stations that do not show evidence for *KS splitting. In general, our results align more closely with the study of Walpole et al. (2014): we also identify 70% of the stations they suggest as null, while this value is below 50% in the Lynner and Long (2013) study. This is likely because the dataset used by Walpole et al. (2014) is significantly larger than that of Lynner and Long (2013), and therefore more comparable to the dataset we are using.

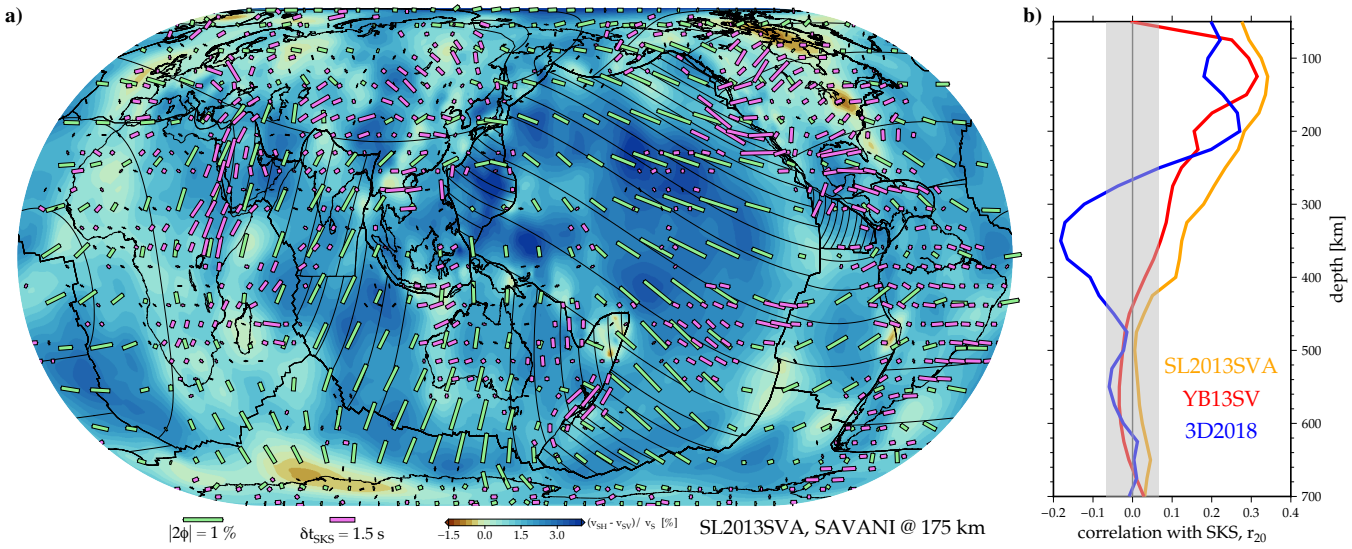

Figure 9. a) Global upper mantle anisotropy from surface wave inversions and *KS splitting. We show radial anisotropy, $\frac{v_{SH}-v_{SV}}{v_S}$, from SAVANI (Auer et al., 2014) in the background, and azimuthal anisotropy from SL2013SVA (Schaeffer and Lebedev, 2013) (green sticks) at 175 km depth, compared to a spherical harmonics fit of the station averaged SKS results (magenta sticks), up to degree $\ell = 20$ (cf. Becker et al., 2007) based on a combination of the Becker et al. (2012) compilation plus our new automated splits. Plate boundaries and absolute velocity contours from NUVEL (DeMets et al., 1994) in black lines, in the spreading-aligned reference frame of Becker et al. (2015), as an approximation of mantle shear (cf. Becker et al., 2014). **b)** Global correlation up to $\ell = 20$ between the updated SKS expansion and surface wave azimuthal anisotropy models SL2013SVA, YB13SV (Yuan and Beghein, 2013), and 3D2018 (Debayle et al., 2016). Gray region shows the range outside of which correlations can be considered significant at the 95% confidence level; figure is an update of the comparison shown in Becker and Lebedev (2021).

Once again, we focus our detailed comparison on the continental United States and southern Canada (Figure 6b). In this region, Walpole et al. (2014) identified numerous null stations, whereas this area was not the focus of Lynner and Long (2013). The null stations identified by Walpole et al. (2014), if not identical, are in the same general regions as those suggested in our study. Walpole et al. (2014) does not suggest null stations in the eastern United States because fewer data were available in this region at the time their study was published (Figure 7b), due to the timing of the USArray deployment.

6 DISCUSSION AND CONCLUSION

We have obtained $90,000$ $\{\phi, \delta t\}$ and $210,000$ null splitting measurements from a seismic dataset that currently contains 16 million three-component seismograms. These are six times more measurements than the largest previous uniformly measured compilation of shear-wave splitting measurements (Walpole et al., 2014). We have conducted a detailed comparison of our results with previous measurements across the United States. Our automatically determined measurements are very similar to those from Liu et al. (2014) and Yang et al. (2017), despite the use of different codes. Our results are also generally similar to the compilation of manual splitting results from Becker et al. (2012). However, some differences to the splitting compilation exist, which can likely be explained by the fact that the results contained in the compilation were obtained using different processing approaches, and at different seismic periods. We determine hundreds of null stations across the globe which are, in general, agreement with the previous results from Walpole et al. (2014).

There are several reasons why we believe that the data product and metadata that we are making publicly available will be a great resource for future research.

(i) The availability of both the metadata and the code package used to conduct the splitting measurements, SplitRacerAUTO (`https://www.geophysik.uni-frankfurt.de/64002762/Software`), ensures that all results can be reproduced. The code version used in this study is also available at `https://doi.org/10.5281/zenodo.14834413` (Wolf et al., 2025).

(ii) Our dataset includes measurements from a vast majority of openly accessible high-magnitude seismic event data. Therefore, it will give a good indication of anisotropy patterns in virtually all regions in which open-access data are available, although regional studies may be able to obtain more *KS measurements than we present in their particular study region; for example, by including lower-magnitude earthquakes.

(iii) The metadata we provide allow the inference of directional information, which is not always possible in current compilations. Therefore, our measurements can be used to determine changes in splitting parameters as a function of backazimuth, which allows detailed regional investigations (e.g., Ritter et al., 2022; Fröhlich et al., 2024).

(iv) Our measurements have been processed uniformly. For example, we used the same seismic periods for each measurement. This makes it possible to calculate sensitivity kernels as needed for anisotropic tomography approaches (e.g., Chevrot, 2006; Link and Long, 2024).

(v) We provide an extensive list of null stations, which are crucial to avoid (often unreliable) explicit anisotropy corrections in both investigations of the upper (e.g., Lynner and Long, 2013; Wolf and Long, 2023) and the lowermost mantle (e.g., Wolf et al., 2023, 2024b).

(vi) We make all diagnostic plots publicly available, implying that all measurements and automatic classifications can be individually assessed.

(vii) This dataset will be occasionally updated as more seismograms are collected as part of the massive dataset collection effort.

ACKNOWLEDGMENTS

JW was funded by the Miller Institute for Basic Research in Science at UC Berkeley. TWB, EG, KHL and JDW received support from the National Science Foundation via grants No. EAR-1927216, EAR-1855624, EAR-1853856, EAR-1853911, and EAR-1830644. The Generic Mapping Tools (Wessel and Smith, 1998) and ObsPy (Beyreuther et al., 2010) were used in this research. JW thanks Barbara Romanowicz and Weiqiang Zhu for their support, and Frederik Link for helpful discussions on SplitRacerAUTO. We thank David Schlaphorst and one anonymous reviewer for constructive feedback.

DATA AVAILABILITY

All data used in this study are publicly available and were collected and pre-processed as part of ASU's global data collection system (`http://adept.sese.asu.edu/`) for their global data products project (`http://swat.sese.asu.edu`). Data were collected from the following on-line data centers: AUSPASS (`https://auspass.edu.au/data.html`), BGR (`https://eida.bgr.de/`), CNDC (`https://www.earthquakescanada.nrcan.gc.ca/stndon/CNDC/index-en.php`),

Earthscope (http://service.iris.edu/), ETH (https://eida.ethz.ch/), FNET (https://www.fnet.bosai.go.jp/top.php?LANG=en), GEOFON (https://geofon.gfz-potsdam.de/) (GFZ Data Services, 1993), GDMS (https://gdmsn.cwb.gov.tw/) (Central Weather Bureau, 2012), ICGC (https://www.icgc.cat/en/Ciutada/Explora-Catalunya/Terratremols), INGV (http://cnt.rm.ingv.it/en/webservices_and_software), IPGP (http://ws.ipgp.fr/) (Institut de physique du globe de Paris (IPGP) and École et Observatoire des Sciences de la Terre de Strasbourg (EOST), 1982), KNMI (http://rdsa.knmi.nl/), KOERI (http://www.koeri.boun.edu.tr/new/en), LMU (http://erde.geophysik.uni-muenchen.de/), NCEDC (https://ncedc.org/) (UC Berkeley Seismological Laboratory, 2014), NIEP (https://www.infp.ro/), NOA (http://bbnet.gein.noa.gr/HL/), ORFEUS (http://www.orfeus-eu.org/), RESIF (https://seismology.resif.fr/) (RESIF, 1995), SCEDC (https://scedc.caltech.edu/) (Caltech, 2014), SSN (http://www.ssn.unam.mx/) (Instituto de Geofísica, Universidad Nacional Autónoma de México, México, 2024), TEXNET (http://rtserve.beg.utexas.edu/), and USP (https://sismo.iag.usp.br/). All networks and network citations are included as Supplementary Information, and were derived from the FDSN network code list (https://fdsn.org/networks/).

All splitting measurements are available as text files in the Supplementary Material. Additionally, measurements can be downloaded at http://swat.sese.asu.edu. Occasional updates will be made available on that website. MATLAB structures with all measurements and matadata that include, for example, the selected time windows and precise event origin times are available at https://doi.org/10.5281/zenodo.14834413 (Wolf et al., 2025). Splitting measurements from Liu et al. (2014), Yang et al. (2017) and Walpole et al. (2014) are available in the corresponding Supplementary Materials. The latest splitting compilation update from Becker et al. (2012) can be downloaded at https://www-udc.ig.utexas.edu/external/becker/sksdata.html.

CODE AVAILABILITY

SplitRacerAUTO (Link et al., 2022) is available at https://www.geophysik.uni-frankfurt.de/64002762/Software. The code version that we used to measure splitting is also available at https://doi.org/10.5281/zenodo.14834413 (Wolf et al., 2025).

References

Ando, M., Ishikawa, Y., Yamazaki, F., 1983. Shear wave polarization anisotropy in the upper mantle beneath Honshu, Japan. Journal of Geophysical Research: Solid Earth 88, 5850–5864. doi:10.1029/JB088iB07p05850.

Auer, L., Boschi, L., Becker, T.W., Nissen-Meyer, T., Giardini, D., 2014. Savani: A variable-resolution whole-mantle model of anisotropic shear-velocity variations based on multiple datasets. Journal of Geophysical Research: Solid Earth 119, 3006–3034. doi:10.1002/2013JB010773.

Becker, T.W., Conrad, C.P., Schaeffer, A.J., Lebedev, S., 2014. Origin of azimuthal seismic anisotropy in oceanic plates and mantle. Earth and Planeteray Science Letters 401, 236–250. doi:10.1016/j.epsl.2014.06.014.

Becker, T.W., Ekström, G., Boschi, L., Woodhouse, J., 2007. Length scales, patterns, and origin of azimuthal seismic anisotropy in the upper mantle as mapped by Rayleigh waves. Geophysical Journal International 171, 451–462.

Becker, T.W., Kellogg, J.B., Ekström, G., O'Connell, R.J., 2003. Comparison of azimuthal seismic anisotropy from surface waves and finite-strain from global mantle-circulation models. Geophysical Journal International 155, 696–714. doi:10.1046/j.1365-246X.2003.02085.x.

Becker, T.W., Kustowski, B., Ekström, G., 2008. Radial seismic anisotropy as a constraint for upper mantle rheology. Earth and Planetary Science Letters 267, 213–237. doi:10.1016/j.epsl.2007.11.038.

Becker, T.W., Lebedev, S., 2021. Dynamics of the Upper Mantle in Light of Seismic Anisotropy. American Geophysical Union (AGU). chapter 10. pp. 257–282. doi:10.1002/9781119528609.ch10.

Becker, T.W., Lebedev, S., Long, M.D., 2012. On the relationship between azimuthal anisotropy from shear wave splitting and surface wave tomography. Journal of Geophysical Research: Solid Earth 117, B01306. doi:10.1029/2011JB008705.

Becker, T.W., Schaeffer, A.J., Lebedev, S., Conrad, C.P., 2015. Toward a generalized plate motion reference frame. Geophysical Research Letters 42, 3188 – 3196. doi:10.1002/2015GL063695.

Becker, T.W., Schulte-Pelkum, V., Blackman, D.K., Kellogg, J.B., O'Connell, R.J., 2006. Mantle flow under the western United States from shear wave splitting. Earth and Planetary Science Letters 247, 235–251. doi:10.1016/j.epsl.2006.05.010.

Behn, M.D., Conrad, C.P., Silver, P.G., 2004. Detection of upper mantle flow associated with the African Superplume. Earth and Planetary Science Letters 224, 259–274. doi:10.1016/j.epsl.2004.05.026.

Bernard, R., Behr, W.M., Becker, T.W., Young, D., 2019. Relationships between olivine CPO and deformation parameters in naturally deformed rocks and implications for mantle seismic anisotropy. Geochemistry, Geophysics, Geosystems doi:10.1002/2019GC008289.

Beyreuther, M., Barsch, R., Krischer, L., Megies, T., Behr, Y., Wassermann, J., 2010. Obspy: A python toolbox for seismology. Seismological Research Letters 81, 530–533. doi:10.1111/10.1785/gssrl.81.3.530.

Bird, P., 2003. An updated digital model of plate boundaries. Geochemistry, Geophysics, Geosystems 4. doi:10.1029/2001GC000252.

Bowman, J.R., Ando, M., 1987. Shear-wave splitting in the upper-mantle wedge above the Tonga subduction zone. Geophys-

ical Journal of the Royal Astronomical Society 88, 25–41. doi:10.1111/j.1365-246X.1987.tb01367.x.

Caltech, 2014. Southern California Earthquake Center. doi:10.7909/C3WD3xH1.

Central Weather Bureau, 2012. Central Weather Bureau Seismographic Network. doi:10.7914/SN/T5.

Chevrot, S., 2000. Multichannel analysis of shear wave splitting. Journal of Geophysical Research: Solid Earth 105, 21579–21590. doi:10.1029/2000JB900199.

Chevrot, S., 2006. Finite-frequency vectorial tomography: a new method for high-resolution imaging of upper mantle anisotropy. Geophysical Journal International 165, 641–657. doi:10.1111/j.1365-246X.2006.02982.x.

Chevrot, S., van der Hilst, R.D., 2003. On the effects of a dipping axis of symmetry on shear wave splitting measurements. Geophysical Journal International 152, 497–505. doi:10.1046/j.1365-246X.2003.01865.x.

Creasy, N., Miyagi, L., Long, M.D., 2020. A Library of Elastic Tensors for Lowermost Mantle Seismic Anisotropy Studies and Comparison With Seismic Observations. Geochemistry, Geophysics, Geosystems 21, e2019GC008883. doi:10.1029/2019GC008883.

Debayle, E., Dubuffet, F., Durand, S., 2016. An automatically updated S-wave model of the upper mantle and the depth extent of azimuthal anisotropy. Geophysical Research Letters 43. doi:10.1002/2015GL067329.

DeMets, C., Gordon, R.G., Argus, D.F., Stein, S., 1994. Effect of recent revisions to the geomagnetic reversal time scale on estimates of current plate motions. Geophysical Research Letters 21, 2191–2194.

Ekström, G., Busby, R., 2008. Measurements of Seismometer Orientation at USArray Transportable Array and Backbone Stations. Seismological Research Letters 79, 554–561. doi:10.1785/gssrl.79.4.554.

Evans, M.S., Kendall, J.M., Willemann, R.J., 2006. Automated SKS splitting and upper-mantle anisotropy beneath Canadian seismic stations. Geophysical Journal International 165, 931–942. doi:10.1111/j.1365-246X.2006.02973.x.

Foley, B.J., Long, M.D., 2011. Upper and mid–mantle anisotropy beneath the Tonga slab. Geophysical Research Letters 38. doi:10.1029/2010GL046021.

Fouch, M.J., Fischer, K.M., Parmentier, E.M., Wysession, M.E., Clarke, T.J., 2000. Shear wave splitting, continental keels, and patterns of mantle flow. Journal of Geophysical Research: Solid Earth 105, 6255–6275. doi:10.1029/1999JB900372.

Fröhlich, Y., Grund, M., Ritter, J.R.R., 2024. Lateral and vertical variations of seismic anisotropy in the lithosphere–asthenosphere system underneath Central Europe from long-term splitting measurements. Geophysical Journal International 239, 112–135. doi:10.1093/gji/ggae245.

Gaboret, C., Forte, A.M., Montagner, J.P., 2003. The unique dynamics of the Pacific hemisphere mantle and its signature on seismic anisotropy. Earth and Planetary Science Letters 208, 219–233. doi:10.1016/S0012-821X(03)00037-2.

GFZ Data Services, 1993. GEOFON Data Centre: GEOFON Seismic Network. doi:10.14470/TR560404.

Hudson, T., Asplet, J., Walker, A., 2023. Automated shear-wave splitting analysis for single- and multi- layer anisotropic media. Seismica 2. doi:10.26443/seismica.v2i2.1031.

Institut de physique du globe de Paris (IPGP), École et Observatoire des Sciences de la Terre de Strasbourg (EOST), 1982. Geoscope, french global network of broad band seismic stations. doi:10.18715/GEOSCOPE.G.

Instituto de Geofísica, Universidad Nacional Autónoma de México, México, 2024. SSN: Servicio Sismológico Nacional. doi:10.21766/SSNMX/SN/MX.

IRIS Transportable Array, 2003. USArray Transportable Array. doi:10.7914/SN/TA.

Kneller, E.A., van Keken, P.E., Karato, S., Park, J., 2005. B-type olivine fabric in the mantle wedge: Insights from high-resolution non-newtonian subduction zone models. Earth and Planetary Science Letters 237, 781–797. doi:10.1016/j.epsl.2005.06.049.

Kocks, U., Tomé, C., Wenk, H., 2000. Texture and Anisotropy: Preferred Orientations in Polycrystals and Their Effect on Materials Properties. Cambridge University Press.

Kong, F., Gao, S.S., Liu, K.H., 2015. A systematic comparison of the transverse energy minimization and splitting intensity techniques for measuring shear-wave splitting parameters. Bulletin of the Seismological Society of America 105, 230–239. doi:10.1785/0120140108.

Lassak, T.M., Fouch, M.J., Hall, C.E., Kaminski, É., 2006. Seismic characterization of mantle flow in subduction systems: Can we resolve a hydrated mantle wedge? Earth and Planetary Science Letters 243, 632–649. doi:10.1016/j.epsl.2006.01.022.

Link, F., Long, M.D., 2024. SItomo – A toolbox for splitting intensity tomography and application in the Eastern Alps. Journal of Geodynamics 159, 102018. doi:10.1016/j.jog.2024.102018.

Link, F., Reiss, M.C., Rümpker, G., 2022. An automatized XKS-splitting procedure for large data sets: Extension package for SplitRacer and application to the USArray. Computers & Geosciences 158, 104961. doi:10.1016/j.cageo.2021.104961.

Liu, K., Elsheikh, A., Lemnifi, A., Purevsuren, U., Ray, M., Refayee, H., Yang, B., Yu, Y., Gao, S., 2014. A uniform database of teleseismic shear wave splitting measurements for the western and central United States. Geochemistry, Geophysics, Geosystems 15, 2075–2085. doi:10.1002/2014GC005267.

Liu, K.H., Gao, S.S., 2013. Making Reliable Shear-Wave Splitting Measurements. Bulletin of the Seismological Society of America 103, 2680–2693. doi:10.1785/0120120355.

Long, M.D., Becker, T., 2010. Mantle dynamics and seismic anisotropy. Earth and Planetary Science Letters 297, 341–354. doi:10.1016/j.epsl.2010.06.036.

Long, M.D., van der Hilst, R.D., 2005. Upper mantle anisotropy beneath japan from shear wave splitting. Physics of the Earth and Planetary Interiors 151, 206–222. doi:10.1016/j.pepi.2005.03.003.

Lynner, C., Long, M.D., 2013. Sub-slab seismic anisotropy and mantle flow beneath the Caribbean and Scotia subduction zones: Effects of slab morphology and kinematics. Earth and Planetary Science Letters 361, 367–378. doi:10.1016/j.epsl.2012.11.007.

Montagner, J.P., 1998. Where can seismic anisotropy be detected in the Earth's mantle? In boundary layers. Pure Appl. Geophys. 151, 223–256.

Montagner, J.P., Griot-Pommera, D.A., Lavé, J., 2000. How to relate body wave and surface wave anisotropy? Journal of Geophysical Research: Solid Earth 105, 19015–19027. doi:10.1029/2000JB900015.

Nicolas, A., Christensen, N.I., 1987. Formation of anisotropy in upper mantle peridotites; a review, in: Fuchs, K., Froidevaux, C. (Eds.), Composition, Structure and Dynamics of the Lithosphere-Asthenosphere system. American Geophysical Union, Washington DC. volume 16 of *Geodynamics*, pp. 111–123.

Nowacki, A., Wookey, J., Kendall, J.M., 2011. New advances in using seismic anisotropy, mineral physics and geodynamics to understand deformation in the lowermost mantle. Journal of Geodynamics 52, 205–228. doi:10.1016/j.jog.2011.04.003.

Reiss, M., Rümpker, G., 2017. SplitRacer: MATLAB Code and GUI for Semiautomated Analysis and Interpretation of Teleseismic Shear-Wave Splitting. Seismological Research Letters 88, 392 — 409. doi:10.1785/0220160191.

Reiss, M.C., Long, M.D., Creasy, N., 2019. Lowermost Mantle Anisotropy Beneath Africa From Differential SKS-SKKS Shear-Wave Splitting. Journal of Geophysical Research: Solid Earth 124, 8540–8564. doi:10.1029/2018JB017160.

RESIF, 1995. RESIF-RLBP French Broad-band network, RESIF-RAP strong motion network and other seismic stations in metropolitan France. doi:10.15778/RESIF.FR.

Ritter, J., Froehlich, Y., Alonso, Y., Grund, M., 2022. Short-scale laterally varying SK(K)S shear wave splitting at BFO, Germany – implications for the determination of anisotropic structures. Journal of Seismology , 1137 – 1156doi:10.1007/s10950-022-10112-w.

Romanowicz, B., Wenk, H.R., 2017. Anisotropy in the deep Earth. Physics of the Earth and Planetary Interiors 269, 58–90. doi:10.1016/j.pepi.2017.05.005.

Rümpker, G., Silver, P.G., 1998. Apparent shear-wave splitting parameters in the presence of vertically varying anisotropy. Geophysical Journal International 135, 790–800. doi:10.1046/j.1365-246X.1998.00660.x.

Russo, R.M., Silver, P.G., 1994. Trench-Parallel Flow Beneath the Nazca Plate from Seismic Anisotropy. Science 263, 1105–1111. doi:10.1126/science.263.5150.1105.

Savage, M.K., 1999. Seismic anisotropy and mantle deformation: What have we learned from shear wave splitting? Reviews of Geophysics 37, 65 – 106. doi:10.1016/10.1029/98RG02075.

Schaeffer, A., Lebedev, S., 2013. Global shear speed structure of the upper mantle and transition zone. Geophys. J. Int. 194, 417–449.

Silver, P.G., 1996. Seismic Anisotropy beneath the Continents: Probing the Depths of Geology. Annual Review of Earth and Planetary Sciences 24, 385 – 432. doi:10.1146/annurev.earth.24.1.385.

Silver, P.G., Chan, W.W., 1991. Shear wave splitting and subcontinental mantle deformation. Journal of Geophysical Research: Solid Earth 96, 16429–16454. doi:10.1029/91JB00899.

Silver, P.G., Savage, M.K., 1994. The Interpretation of Shear-Wave Splitting Parameters In the Presence of Two Anisotropic Layers. Geophysical Journal International 119, 949–963. doi:10.1111/j.1365-246X.1994.tb04027.x.

Tanimoto, T., Anderson, D.L., 1984. Mapping convection in the mantle. Geophysical Research Letters 11, 287–290. doi:10.1029/GL011i004p00287.

Teanby, N.A., Kendall, J.M., Van der Baan, M., 2004. Automation of shear-wave splitting measurements using cluster analy-

sis. Bulletin of the Seismological Society of America 94, 453–463. doi:10.1785/0120030123.

UC Berkeley Seismological Laboratory, 2014. Northern California Earthquake Data Center. doi:10.7932/NCEDC.

Vecsey, L., Plomerová, J., Babuška, V., 2008. Shear-wave splitting measurements — problems and solutions. Tectonophysics 462, 178–196. doi:https://doi.org/10.1016/j.tecto.2008.01.021. seismic Anisotropy and Geodynamics of the Lithosphere-Asthenosphere System.

Vinnik, L., Kosarev, G.L., Makeyeva, L.I., 1984. Anisotropy of the lithosphere from the observations of SKS and SKKS phases. Proc. Acad. Sci. USSR 278, 1335–1339.

Walpole, J., Wookey, J., Masters, G., Kendall, J.M., 2014. A uniformly processed data set of SKS shear wave splitting measurements: A global investigation of upper mantle anisotropy beneath seismic stations. Geochemistry, Geophysics, Geosystems 15, 1991–2010. doi:10.1002/2014GC005278.

Walsh, E., Arnold, R., Savage, M.K., 2013. Silver and Chan revisited. Journal of Geophysical Research: Solid Earth 118, 5500–5515. doi:10.1002/jgrb.50386.

Wessel, P., Smith, W.H.F., 1998. New, improved version of generic mapping tools released. Eos, Transactions American Geophysical Union 79, 579–579. doi:10.1029/98EO00426.

Wirth, E., Long, M.D., 2010. Frequency-dependent shear wave splitting beneath the Japan and Izu-Bonin subduction zones. Physics of the Earth and Planetary Interiors 181, 141–154. doi:10.1016/j.pepi.2010.05.006.

Wolf, J., Becker, T.W., Garnero, E., Liu, K.H., West, J.D., 2025. Additional data/codes concerning "Comprehensive global dataset of uniformly processed shear-wave splitting measurements". doi:10.5281/zenodo.14834413.

Wolf, J., Li, M., Long, M.D., Garnero, E., 2024a. Advances in mapping lowermost mantle convective flow with seismic anisotropy observations. Reviews of Geophysics 62, e2023RG000833. doi:10.1029/2023RG000833.

Wolf, J., Long, M., 2024. ScS shear-wave splitting in the lowermost mantle: Practical challenges and new global measurements. Seismica doi:10.26443/seismica.v3i1.1128.

Wolf, J., Long, M.D., 2022. Slab-driven flow at the base of the mantle beneath the northeastern Pacific Ocean. Earth and Planetary Science Letters 594, 117758. doi:10.1016/j.epsl.2022.117758.

Wolf, J., Long, M.D., 2023. Upper Mantle Anisotropy and Flow Beneath the Pacific Ocean Revealed by Differential PS-SKS Splitting. Geophysical Research Letters 50, e2023GL104402. doi:10.1029/2023GL104402.

Wolf, J., Long, M.D., Creasy, N., Garnero, E., 2023. On the measurement of Sdiff splitting caused by lowermost mantle anisotropy. Geophysical Journal International doi:10.1093/gji/ggac490.

Wolf, J., Long, M.D., Frost, D.A., 2024b. Ultralow velocity zone and deep mantle flow beneath the Himalayas linked to subducted slab. Nature Geoscience , 1–7doi:10.1038/s41561-024-01386-5.

Wolf, J., Long, M.D., Frost, D.A., Nissen-Meyer, T., 2024c. The expression of mantle seismic anisotropy in the global seismic wavefield. Geophysical Journal International 238, 346–363. doi:10.1093/gji/ggae164.

Wolf, J., Long, M.D., Leng, K., Nissen-Meyer, T., 2022. Constraining deep mantle anisotropy with shear wave splitting measurements: Challenges and new measurement strategies. Geophysical Journal International 230, 507–527. doi:10.

1093/gji/ggac055.

Wolfe, C.J., Solomon, S.C., 1998. Shear-Wave Splitting and Implications for Mantle Flow Beneath the MELT Region of the East Pacific Rise. Science 280, 1230–1232. doi:10.1126/science.280.5367.1230.

Wookey, J., Kendall, J.M., 2008. Constraints on lowermost mantle mineralogy and fabric beneath Siberia from seismic anisotropy. Earth and Planetary Science Letters 275, 32–42. doi:10.1016/j.epsl.2008.07.049.

Wüstefeld, A., Al-Harrasi, O., Verdon, J.P., Wookey, J., Kendall, J.M., 2010. A strategy for automated analysis of passive microseismic data to image seismic anisotropy and fracture characteristics. Geophysical Prospecting 58, 755–773. doi:10.1111/j.1365-2478.2010.00891.x.

Wüstefeld, A., Bokelmann, G., 2007. Null detection in shear-wave splitting measurements. Bulletin of the Seismological Society of America 97, 1204–1211. doi:10.1785/0120060190.

Wüstefeld, A., Bokelmann, G., Zaroli, C., Barruol, G., 2008. Splitlab: A shear-wave splitting environment in MATLAB. Computers & Geosciences 34, 515–528. doi:10.1016/j.cageo.2007.08.002.

Wüstefeld, A., Bokelmann, G.H.R., Barruol, G., Montagner, J.P., 2009. Identifying global seismic anisotropy patterns by correlating shear-wave splitting and surface-wave data. Physics of the Earth and Planetary Interiors 176, 198–212. Database at www.gm.univ-montp2.fr/splitting/DB/, accessed 11/2024.

Yamazaki, D., Karato, S., 2001. High-pressure rotational deformation apparatus to 15 GPa. Review of Scientific Instruments 72, 4207–4211. doi:10.1063/1.1412858.

Yang, B., Liu, Y., Dahm, H., Liu, K., Gao, S., 2017. Seismic azimuthal anisotropy beneath the eastern United States and its geodynamic implications. Geophysical Research Letters , 2670–2678doi:10.1002/2016GL071227.

Yuan, K., Beghein, C., 2013. Seismic anisotropy changes across upper mantle phase transitions. Earth and Planetary Science Letters 374, 132–144.

Geophys. J. Int. (2024) **2024**, 1–22

Comprehensive global dataset of uniformly processed shear-wave splitting measurements

Jonathan Wolf[1,2⋆], Thorsten W. Becker[3,4,5], Edward Garnero[6], Kelly H. Liu[7], John D. West[6]

[1] *Department of Earth and Planetary Science, University of California, Berkeley, CA, USA*
[2] *Miller Institute for Basic Research in Science, Berkeley, CA, USA*
[3] *Institute for Geophysics, Jackson School of Geosciences, The University of Texas at Austin, TX, USA*
[4] *Department of Earth and Planetary Sciences, Jackson School of Geosciences, The University of Texas at Austin, TX, USA*
[5] *Oden Institute for Computational Engineering & Sciences, The University of Texas at Austin, TX, USA*
[6] *School of Earth and Space Exploration, Arizona State University, Tempe, AZ, USA*
[7] *Department of Earth Sciences and Engineering, Missouri University of Science and Technology, Rolla, MO, USA*

February 13, 2025

SUMMARY

Seismic anisotropy can inform us about convective flow in the mantle. Shear waves traveling through azimuthally anisotropic regions split into fast and slow pulses, and measuring the resulting shear-wave splitting provides some of the most direct insights into Earth's interior dynamics. Shear-wave splitting is a constraint for path-averaged azimuthal anisotropy and is often studied regionally. **G**lobal compilations of these measurements **also** exist. Such compilations include measurements obtained using different data processing methodologies (e.g., filtering), which do not necessarily yield identical results, and reproducing a number of studies can be challenging given that not all provide the required information, e.g., about the source location. Here, we automatically determine SKS, SKKS and PKS shear-wave splitting parameters from a global dataset. This dataset includes all earthquakes with magnitudes ≥ 5.9 from 2000 to the present, collected from 24 data centers, totaling over 4,700 events and 16 million three-component seismograms. We obtain approximately 90,000 robust measurements for "fast azimuth", ϕ, and delay time, δt, and 210,000 robust null measurements. Results generally agree with previous work but our measurements allow us to identify hundreds of "null stations" below which the mantle appears effectively isotropic with respect to azimuthal anisotropy, which are important for some splitting techniques. We make all measurements publicly available as a data product, along with detailed metadata. This serves two purposes: ensuring full reproducibility of results and providing all necessary information for future systematic use of our measurements, in tomography applications or comparisons with geodynamic flow predictions.

Key words: Shear-wave splitting – Global compilation – Seismic anisotropy – Mantle flow.

1 INTRODUCTION

Seismic anisotropy refers to the phenomenon **by** which seismic waves travel at different velocities depending on their propagation direction and/or polarization. In the mantle, anisotropy arises due to two primary mechanisms which can both be linked to Earth's internal deformation and convective evolution: (1) Crystallographic-preferred orientation (CPO), where intrinsically anisotropic mineral crystals align under finite deformation with their directional elastic properties, and (2) shape-preferred

⋆ jonathan.wolf@berkeley.edu

orientation (SPO), involving aligned isotropic or anisotropic materials, e.g., layered composites, that can be effectively anisotropic on the scales seen by the dominant seismic wavelength (e.g., Nicolas and Christensen, 1987; Silver, 1996; Kocks et al., 2000; Long and Becker, 2010; Romanowicz and Wenk, 2017). The detection and characterization of seismic anisotropy can provide valuable information on convective flow in Earth's mantle (e.g., Tanimoto and Anderson, 1984; Gaboret et al., 2003; Becker et al., 2003; Nowacki et al., 2011; Wolf et al., 2024a). For the typical, "A" type CPOs of olivine, as they might form under dislocation creep in the upper mantle, the fast propagation direction of upper mantle anisotropy is expected to align with shear in mantle flow. Different alignments might be caused by high volatile and/or stress type CPO formation (e.g., Kneller et al., 2005; Lassak et al., 2006; Becker et al., 2008), although those fabrics appear less common and less systematic in the rock record (e.g., Bernard et al., 2019). However, in the deepest mantle, the relationship between anisotropy and flow is more complicated (e.g., Yamazaki and Karato, 2001; Wookey and Kendall, 2008; Creasy et al., 2020); it cannot necessarily be assumed the polarization direction of the fast traveling wave corresponds to the direction of convective flow (e.g., Yamazaki and Karato, 2001; Nowacki et al., 2011; Wolf and Long, 2022). Seismic anisotropy is usually stronger in the upper than in the lowermost mantle (e.g., Romanowicz and Wenk, 2017; Becker and Lebedev, 2021). Therefore, fast directions of shear wave splitting measurements are routinely interpreted as being due to upper mantle flow (e.g., Silver, 1996; Fouch et al., 2000; Behn et al., 2004; Becker et al., 2006).

The SKS, SKKS and PKS (Figure 1**a**) seismic phases, hereafter referred to as *KS, are SV polarized upon reentry into the mantle from the outer core. If a *KS wave travels through an anisotropic region in the receiver-side mantle, it splits into two pulses, one of which travels faster than the other. This phenomenon can occur in Earth's upper mantle, as schematically shown in Figure 1**b**. The two components (red and blue in Figure 1**b**) accumulate a time lag, or relative delay time, δt, which increases as a function of the distance traveled through the anisotropic material. We denote the polarization orientation of the fast pulse, or "fast axis", as ϕ (counted clockwise from the North; Figure 1**c**). These two parameters characterize seismic anisotropy for a typical shear wave splitting measurement (Ando et al., 1983; Vinnik et al., 1984; Silver and Chan, 1991).

Shear wave splitting parameters $\{\phi, \delta t\}$ are typically determined through manual or semi-automated inspection and analysis of data (e.g., Teanby et al., 2004; Wüstefeld et al., 2010, 2008; Reiss and Rümpker, 2017), although fully automated approaches have also been applied (e.g., Evans et al., 2006; Liu et al., 2014; Walpole et al., 2014; Link et al., 2022; Hudson et al., 2023). Results from these manual analyses as well as those derived from automatic approaches have been compiled into large splitting parameter collections (e.g., Silver, 1996; Wüstefeld et al., 2009). These compilations have provided valuable insights into upper mantle flow and have enabled detailed comparisons between shear-wave splitting (from *KS body waves) and surface wave wave inversions (e.g., Montagner et al., 2000; Wüstefeld et al., 2009; Becker et al., 2012). However, global compilations include splitting parameters from studies that use different data processing techniques, which can vary depending on the periods used in analyses and the methods employed to calculate splitting parameters (Savage, 1999; Long and van der Hilst, 2005; Vecsey et al., 2008; Kong et al., 2015). Additionally, some studies do not provide specific information on the earthquake data used to determine splitting parameters, making it challenging (if not impossible) to reproduce their results, or

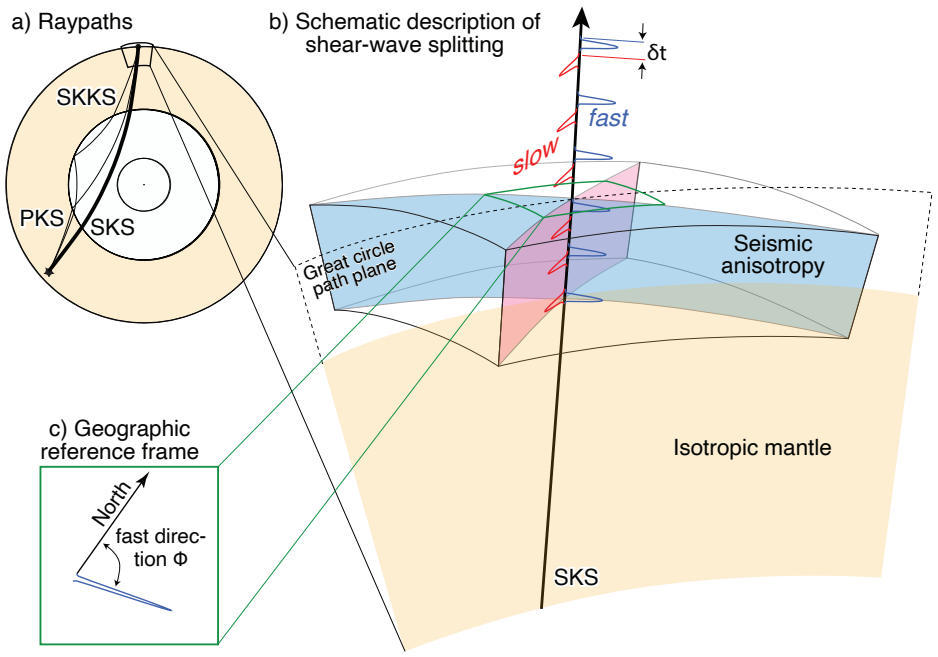

Figure 1. Schematic representation of shear-wave splitting due to upper mantle anisotropy. **a) Schematic Earth cross-section showing PKS, SKS and SKKS (*KS) raypaths. (b) In presence of seismic anisotropy in the upper mantle, *KS splits into fast (blue) and slow (red) traveling components with mutually orthogonal polarizations. These components accumulate a relative time lag (δt); additionally, the fast polarization direction can be measured. (c) Fast polarization direction ϕ relative to geographic north.**

to analyze features such as backazimuthal dependence of ϕ and δt which can provide insights into the nature of anisotropy at depth (e.g., Silver and Savage, 1994; Rümpker and Silver, 1998; Chevrot and van der Hilst, 2003).

Here we automatically measure shear-wave splitting for all earthquakes with magnitudes $\geq$ 5.9 from the year 2000 to present, which were collected from 24 data centers worldwide. We obtain approximately 90,000 well-constrained sets of $\{\phi, \delta t\}$ pairs and 210,000 null measurements. This automatic measurement database is substantially larger than previous ones (e.g., Liu et al., 2014; Walpole et al., 2014). The measurements are compared to existing databases and previous automatic splitting efforts and found generally consistent with previous results. We identify hundreds **of** stations worldwide at which a large majority of *KS waves is unsplit, which are called null stations. Null measurements, at which waves appear not influenced by azimuthal seismic anisotropy in the mantle, provide important information (e.g., Wüstefeld and Bokelmann, 2007; Walpole et al., 2014). Effective "null stations" are essential for the application of some splitting strategies, such as determining S-wave source-side anisotropy (e.g., Russo and Silver, 1994; Foley and Long, 2011; Lynner and Long, 2013), PS bounce point anisotropy (e.g., Wolf et al., 2024c), and inferring lowermost mantle anisotropy from ScS and S_{diff} waves (e.g., Wolf and Long, 2024; Wolf et al., 2022).

The code we use to measure shear-wave splitting is publicly available, and we publish our uniformly processed measurements as well as metadata. This enables reproducibility and the extraction of information such as backazimuthal dependence of splitting parameters. We anticipate that this work will enable new inquiries into Earth's dynamic interior processes using uniformly made measurements from a large global dataset.

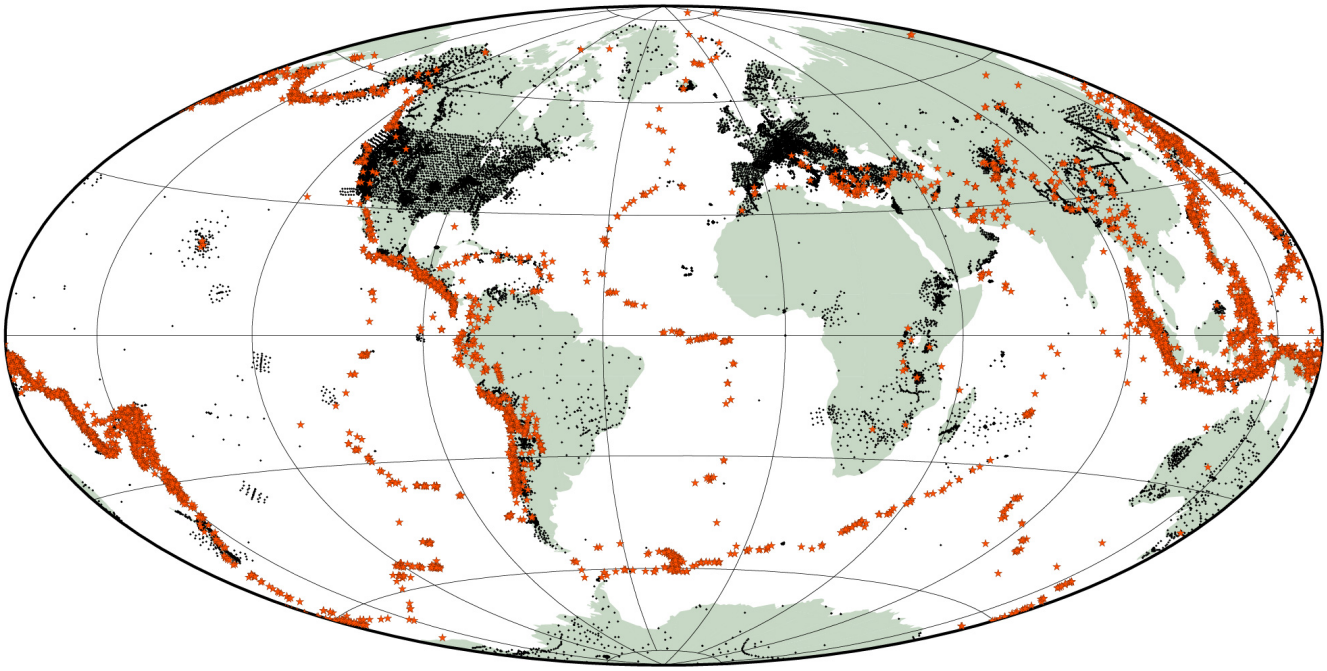

Figure 2. Source-receiver configuration used in this study. Stations are shown as black circles and events as orange stars. We use data from approximately 4,700 different events and 25,000 distinct stations.

2 DATASET AND PRE-PROCESSING

We have collected (and continue collecting) all available data from 24 global data centers from January 1, 2000, to present, for all seismic events with moment magnitudes 5.9 and above (hereafter referred to as the ADEPT dataset, `http://adept.sese.asu.edu/`). We collect 2 hours of data for all stations, instrument deconvolve the data to displacement, rotate the horizontal components to radial and transverse motions, and downsample the seismograms to 20 samples per second. We store the data locally in event-based directories. To date, we have collected over 4700 earthquakes (and over 16 million three-component earthquake recordings). All events and stations that are included in the dataset are shown in Figure 2. The corresponding ~ 500 seismic networks and their citations are provided in the Supplementary Material.

3 SHEAR-WAVE SPLITTING MEASUREMENTS

We conduct shear-wave splitting measurements using the **SplitRacerAUTO MATLAB** code (Reiss and Rümpker, 2017; Link et al., 2022). **SplitRacerAUTO** uses the transverse energy minimization technique (Silver and Chan, 1991) with the uncertainty quantification by Walsh et al. (2013) to determine ϕ and δt. This is repeated for a certain number (we choose 30) of randomly selected time intervals around the expected phase arrival, and measurements are only used if they are robust across all time windows. **The details of this procedure are described in the original publication by Reiss and Rümpker (2017). SplitRacerAUTO** additionally calculates the splitting intensity SI (Chevrot, 2000), which can be expressed as $SI \approx \delta t \sin(2(\alpha - \phi))$, where α is the backazimuth for *KS phases.

The first step of **SplitRacerAUTO** is to conduct data preprocessing **all selected data. We use PKS waves measured at**

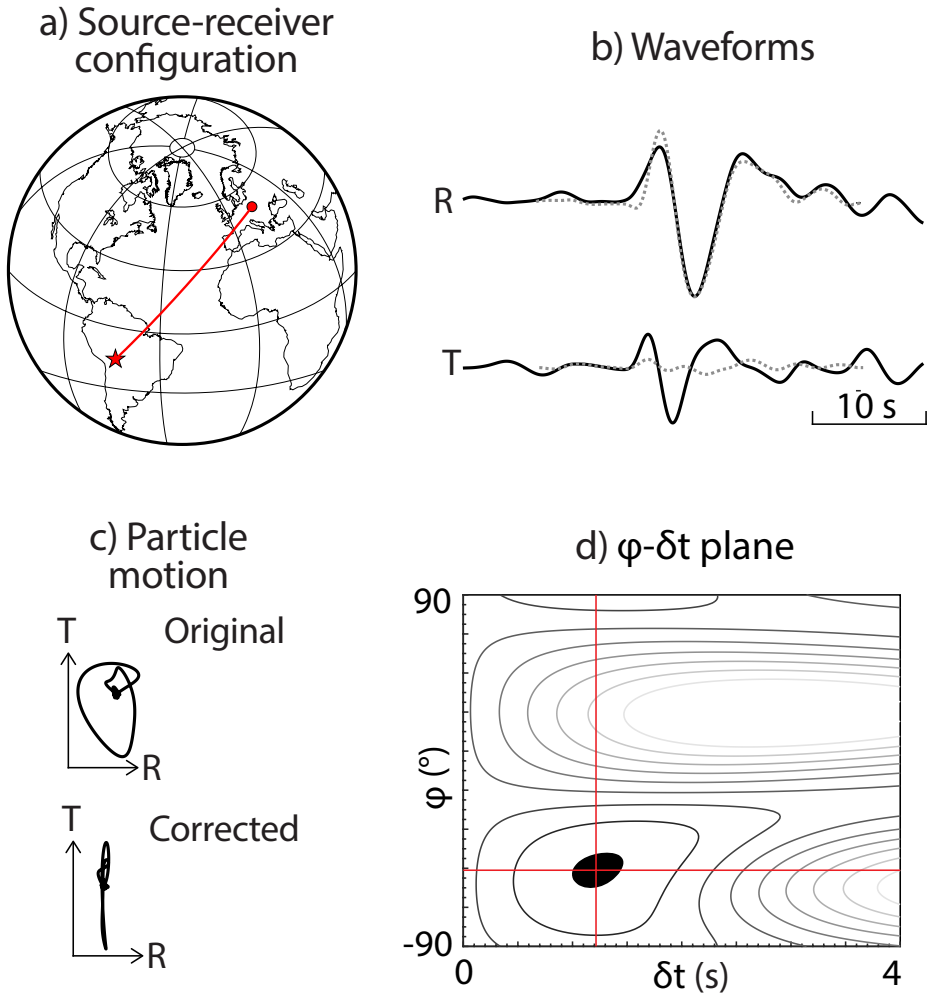

Figure 3. Example of a shear-wave splitting measurement. (a) Event (red star) that occurred on November 22, 2011, beneath central Bolivia and station OJC (red circle) located in Poland. The great-circle path is shown as a red line. (b) Radial (R) and transverse (T) component displacement waveforms. **Waveforms corrected for the best-fitting splitting parameters are shown as gray dotted lines.** (c) Particle motions (radial vs. transverse amplitude) for the original waveform (top) after after correction for the best-fitting splitting parameters (bottom). (d) Best-fitting splitting parameters in the ϕ-δt-plane. Black region indicates 95% confidence interval. The best-fitting ϕ and δt values are indicated by a red line. Contour lines show different transverse energy component levels.

epicentral distances from their inception and $< 155°$**, SKS at distances** $> 85°$ **to their maximum distance, and SKKS at distances** $> 100°$ **to their maximum distance. In the preprocessing, SplitRacerAUTO discards** data with low signal-to-noise ratios (SNRs). SNRs are calculated using an effective horizontal component ($\sqrt{R(t)^2 + T(t)^2}$, R(t)=radial component, T(t)=transverse component), and comparing the mean amplitude of a noise window with the signal window. The noise window is 20 s long and ends 5 s prior to the PREM-predicted arrival time. We set an SNR threshold of 2.2 after applying a **butterworth** bandpass filter **of order 2** to retain periods between 6 and 25 s. Next, **SplitRacerAUTO** uses an additional quality-control algorithm to identify the time window in which the *KS phase under study arrives, avoiding *KS phases that coincide S, ScS and S_{diff} arrivals. In the third step, shear-wave splitting parameters are calculated, and measurements are automatically classified. For more details about **SplitRacerAUTO**, we refer to Link et al. (2022), which includes a thorough benchmark against measurements for which time windows were manually selected and measurements visually classified.

Several modifications have been made to the original code to tailor it for our purposes. We adjust **SplitRacerAUTO**

to read data from event-based directories instead of station-based ones. This data is already rotated into a radial-transverse coordinate frame based on station metadata. To enhance computational speed, which is essential given the large number of seismograms used in this study, we downsample all data to 3 samples per second instead of 20 (that **SplitRacerAUTO** uses per default). We also found that null measurements can be reliably identified using a single time window. Therefore, if a splitting measurement is null, we do not analyze additional time windows. The same applies if the splitting in the first time window is classified as clearly poor. Although these adjustments are minor and do not impact **SplitRacerAUTO**'s core functionality, they increase computational speeds by a factor of about 200. **Our slightly adjusted SplitRacerAUTO version can be found at** `https://doi.org/10.5281/zenodo.14834413` **(Wolf et al., 2025).**

Figure 3 illustrates an example of an SKS shear-wave splitting measurement from data collected at station OJC in Poland, for an event that occurred on November 22, 2011 beneath central Bolivia. In this example, the SKS signal is clearly above the noise level (Figure 3b), the original particle motion is elliptical, and after correcting for the best-fitting splitting parameters, the particle motion becomes linear (Figure 3c). The best-fitting $\{\phi, \delta t\}$ (Figure 3d) splitting parameters are tightly constrained.

SplitRacerAUTO assigns several categories to measurements: good, average, null, and poor. The criteria used for these categorizations are detailed by Link et al. (2022), and we apply the same criteria in this study to assign 'good' and 'average' labels to our *KS splitting measurements. **These criteria include maximum permissible error bars on δt, minimum required energy reductions for the corrected traces and minimum permissible eigenvalue ratios of the calculated covariance matrix.** However, we define null measurements less strictly than Link et al. (2022): we label measurements as 'null' if $|SI| < 0.3$ (instead of < 0.15) and the ratio of the first and second eigenvalues of the covariance matrix is < 0.1 (instead of < 0.06). The decision on how narrowly to define a null measurement is somewhat arbitrary; we adopt this broader SI range for a null definition for practical reasons. Measurements with $|SI| < 0.3$ do not yield well-constrained $\{\phi, \delta t\}$ values because the splitting is too weak (at the periods we are using). Defining these measurements as null allows us to measure splitting for only one time window, thereby not unnecessarily straining our computational resources. **In practice, this definition of null measurements has no influence on the determination of null stations, which are often defined by a percentage of unsplit waves measured at them (e.g., Walpole et al., 2014). In this study, we set a higher threshold for the percentage of nulls required to define null stations compared to previous studies. This approach explicitly accounts for weakly split waves that meet our quality criteria but would likely have been discarded as poor in previous studies.**

4 RESULTS

4.1 Global splitting measurements

We obtain $64{,}154$ SKS, $14{,}439$ SKKS, and $8{,}153$ PKS global $\{\phi, \delta t\}$ measurements. These results are presented in Figure 4 in a global overview, and Figure 5 for regional example zoom-ins.

The overall measurement coverage is largely determined by the station distribution (Figure 2), and consequently, the availability of publicly accessible seismic data that is part of ADEPT. For example, the measurement density is very high in

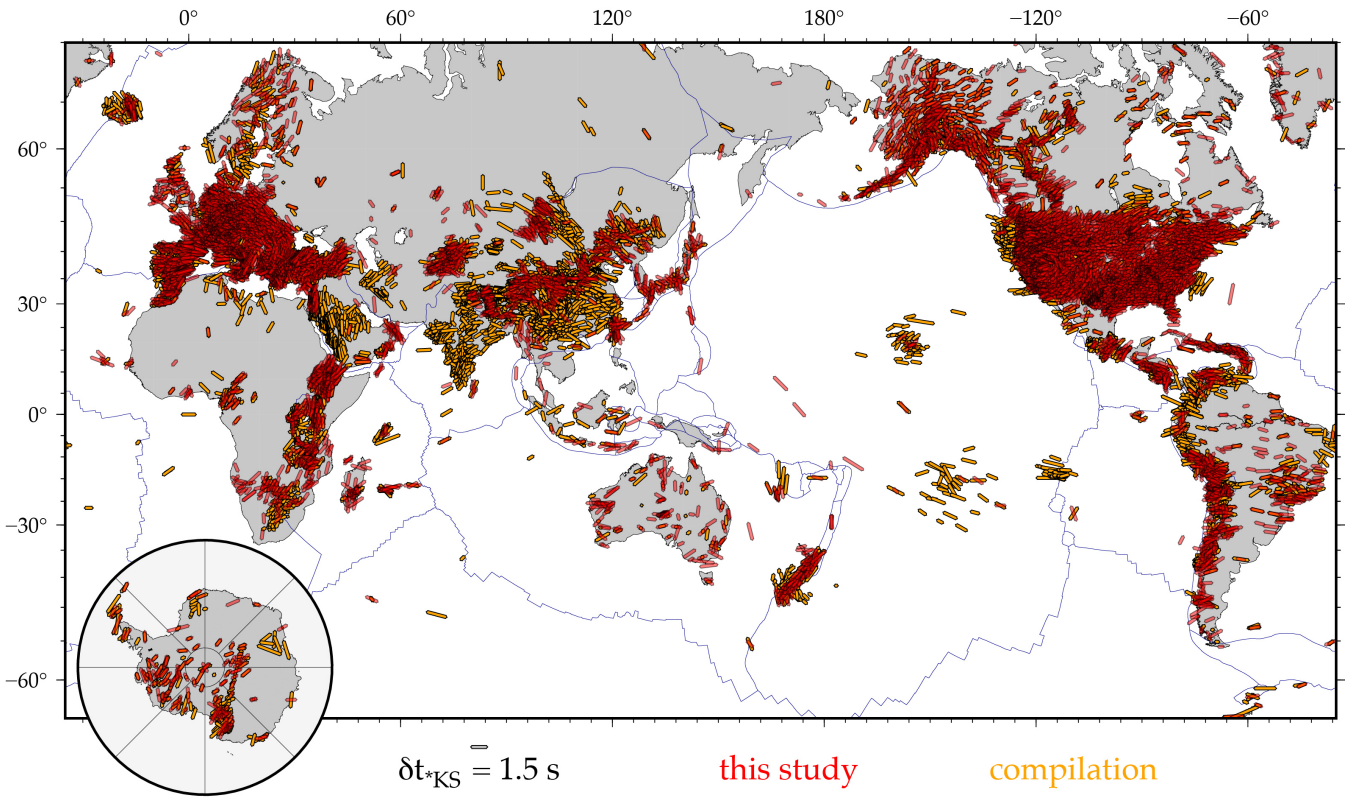

Figure 4. Comparison of global splitting coverage and fast directions between this study (red sticks) and the updated compilation from Becker et al. (2012) (orange sticks, including the Montpellier database of Wüstefeld et al. (2009) with last updates from 2020), with plate boundaries from Bird (2003) in blue. Results for Antarctica are shown as an inset; see Figure 5 and Figure 7 for regional zoom ins. The compilation includes results from restricted data in China, India and Saudi Arabia, leading to better coverage in these regions. Our study adds more coverage in northern Europe, Australia, southern Africa, central Asia and a stretch of Chile.

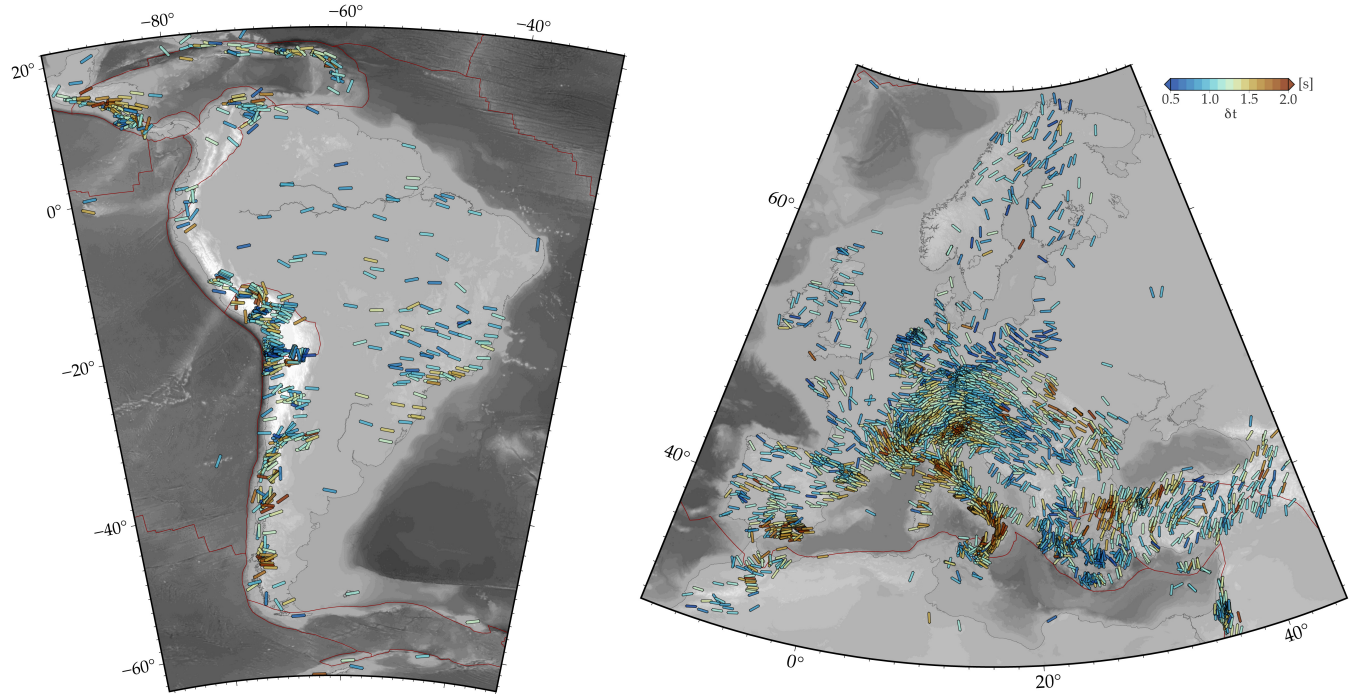

Figure 5. Regional $\{\phi, \delta t\}$ measurement results from our automated analysis for South America (left) and Europe (right). Colored sticks are centered at the station at which splitting was measured. Their orientation indicates the polarization direction ϕ and the color scale represents the delay time δt (legend). Plate boundaries from Bird (2003).

the United States and Europe, while significantly fewer measurements are available for stations in Russia and India. Outside of Europe and North America, countries such as Chile, Japan, Taiwan, New Zealand, Tajikistan, and Kyrgyzstan are particularly well sampled.

4.2 Null measurements

In addition to the splitting parameters $\{\phi, \delta t\}$, we identify which measurements are unsplit or null. Stations where a large majority of records show no splitting are often referred to as null stations, yet this is important information, as noted above. We introduce two distinct categories of null stations. If at least 97.5 % of the records at a station are unsplit, and the station is sampled from more than one 30°-wide azimuth, the station is assigned a null category label A. If between 95.0 % and 97.5 % of the measurements are null, the station is classified as category B. For a station to be included in either of these categories, it must have more than 30 null or $\{\phi, \delta t\}$ measurements. Figure 6 shows null stations as colored circles for category A and as gray circles for category B. The color of the circle indicates how many 30° backazimuthal bins (starting at backazimuth = 0°) contain measurements. In total, we identify 178 category A and 371 category B null stations, many of which are located in the United States and Europe (Figure 6**b,c**).

4.3 Data product description

We make the global $\{\phi, \delta t\}$ and null measurements publicly available. For each phase (SKS, SKKS, PKS), we provide a .txt file that includes the following information: event name, for example '200001081647', corresponding to an event that occurred on January 8, 2000 at 4:47pm UTC; event latitude (°); event longitude (°); event depth (km); station name; network name; station latitude (°); station longitude (°); quality tag; δt (s); δt upper error bound (s); δt lower error bound (s); ϕ (°); ϕ upper error bound (°); ϕ lower error bound (°); splitting intensity; splitting intensity upper error bound; splitting intensity lower error bound. These measurements are also available on the data product website associated with this large data collection effort, `http://swat.sese.asu.edu`. Measurements will occasionally be updated on the website as the ADEPT dataset continues to grow.

For each $\{\phi, \delta t\}$ and null measurement used in this study, we provide diagnostic splitting plots at `http://swat.sese.asu.edu`. These graphics, minimally edited from **SplitRacerAUTO**, include the waveforms, particle motions, ϕ-δt energy maps (similar to Figure 3b-d) and histograms that show the robustness of the splitting measurements across multiple time windows. These graphical products enable researchers to visually evaluate each splitting measurement for their own use.

Additionally, we include .txt files in the Supplementary Information with both category A and B null measurements. The format of these files is: station name, event name, number of robust measurements at the station, station latitude (°), station longitude (°).

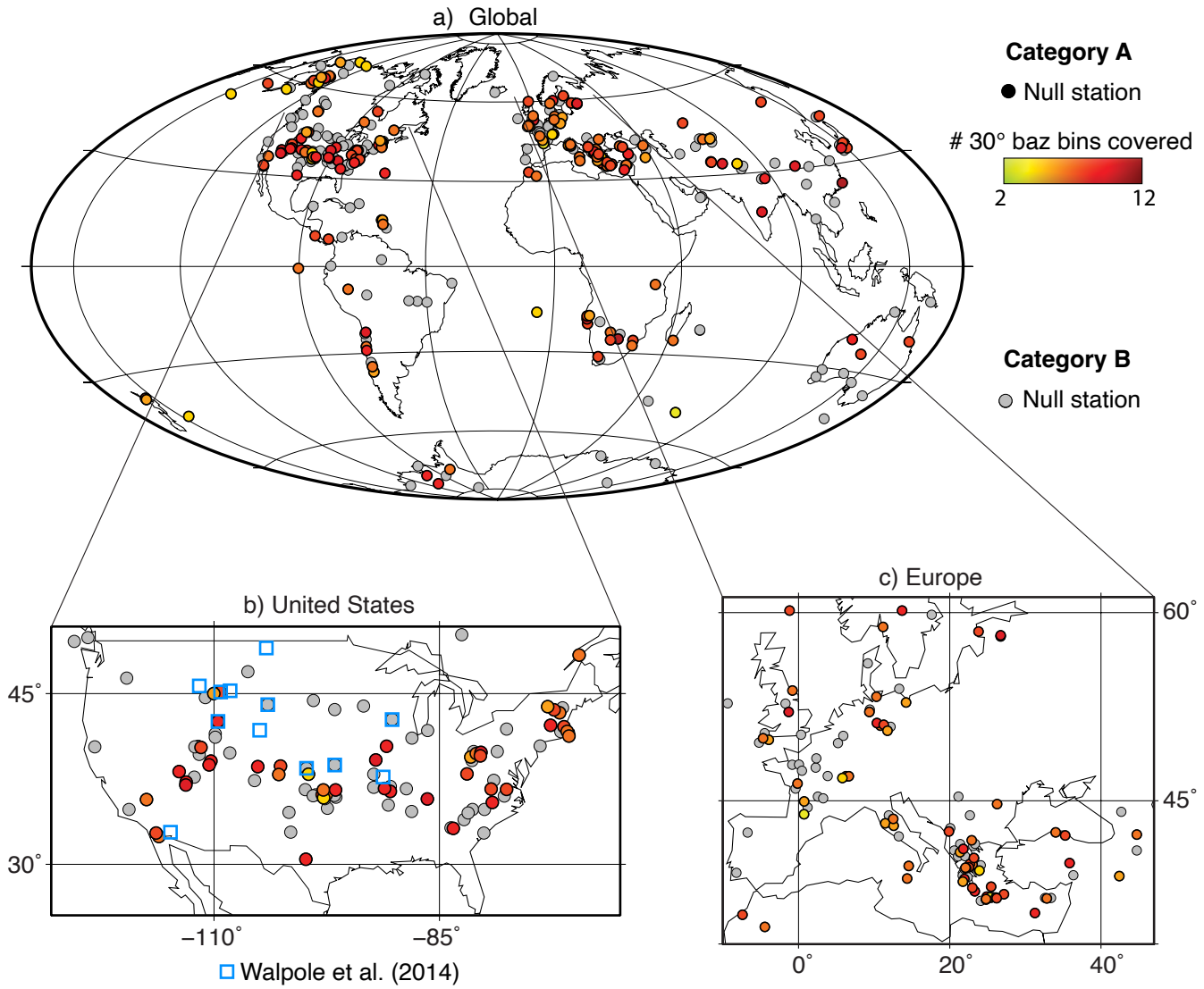

Figure 6. Null stations identified in this study. Category A null stations (stations where $> 97.5\%$ of measurements are null, which show sampling from 2 or more 30° backazimuthal bins) are represented as colored circles, the color scale legend indicates the number of 30° backazimuthal bins from which measurements were obtained. Category B null stations (stations having between 95% and 97.5% null measurements) are displayed as gray circles. **(a) All null stations. (b) Zoom-in centered on the United States with null stations from Walpole et al. (2014) shown as blue squares. (c) Zoom-in centered on Europe.**

5 COMPARISONS TO PREVIOUS STUDIES

5.1 Fast directions and delay times across the continental United States

We focus on the continental United States and its surrounding regions to compare our results with those of previous studies. This region is chosen for its exceptionally dense station coverage, primarily due to the prior deployment of USArray (IRIS Transportable Array, 2003), and because several automatic splitting approaches have been applied here (e.g., Walpole et al., 2014; Liu et al., 2014; Yang et al., 2017; Link et al., 2022). Specifically, we conduct a detailed comparison of our results with the updated composite compilation of manually picked splitting measurements by Becker et al. (2012) which includes the Montpellier database of Wüstefeld et al. (2009) with last updates from 2020, and the automatic measurements by Walpole

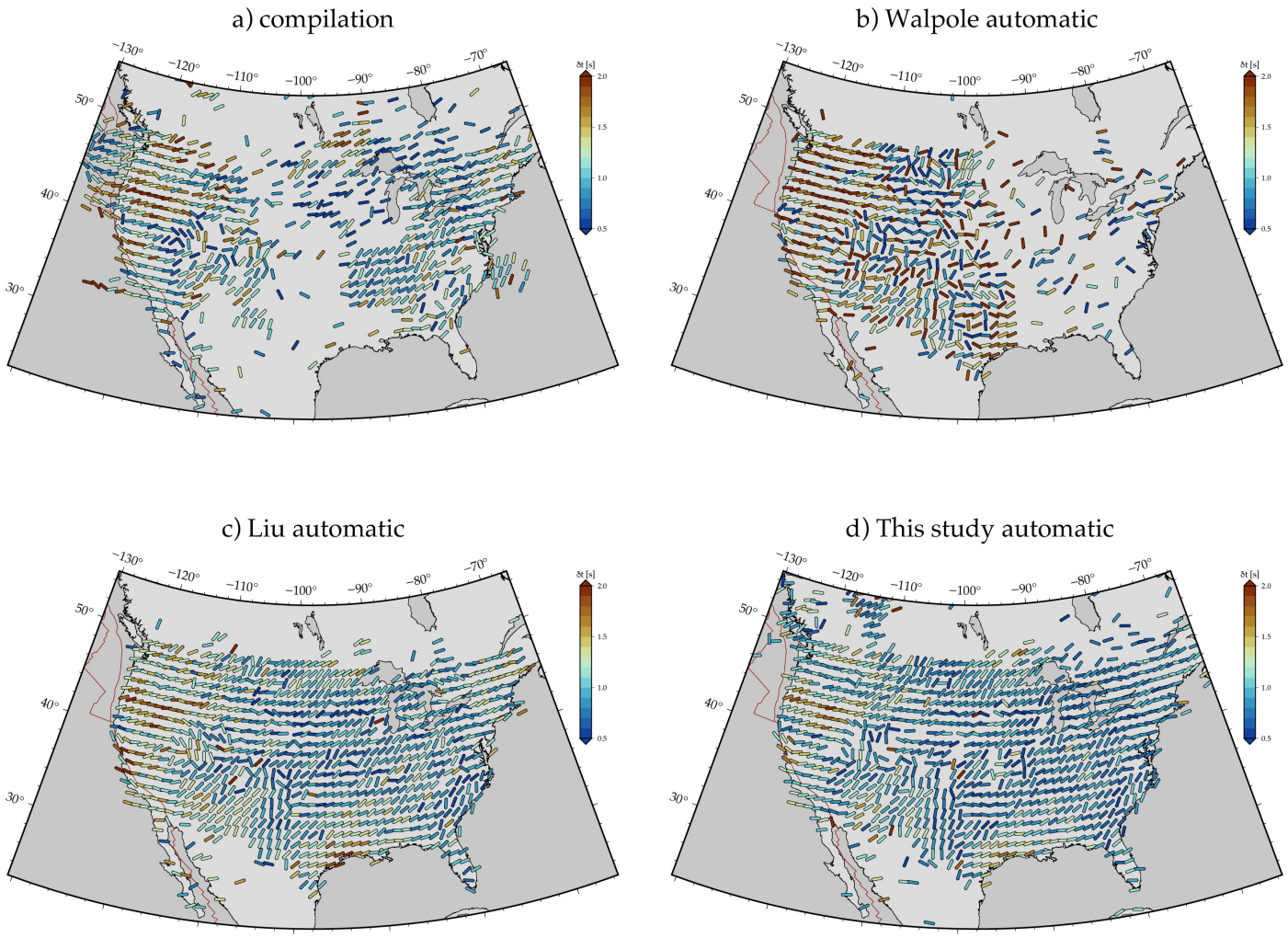

Figure 7. Averaged ($1^\circ \times 1^\circ$ bins) shear-wave splitting parameters across the continental United States and the surrounding regions. Results are shown for (a) the updated compilation of manually measured splitting parameters from Becker et al. (2012) which includes the Montpellier database of Wüstefeld et al. (2009) with last updates from 2020, (b) results from the global automated analysis by Walpole et al. (2014), (c) the automatic USArray results from Liu et al. (2014) and Yang et al. (2017), and, (d) this study. Colored sticks are centered at the station at which splitting was measured. Their orientation indicates the polarization direction ϕ and the color scale represents the delay time δt (legend).

et al. (2014) who provided a global database, as well as automated splits from Liu et al. (2014) and Yang et al. (2017) which are restricted to North America/USArray.

For comparative analysis, we first calculate the station average and then spatially average **these** splits, but we note that backazimuthal information is retained in the original databases. **All averaging is based on delay-time weighted, orientational (i.e., 180° periodic) vector means, and computing the median values within spatial bins.** We show $1^\circ \times 1^\circ$ splitting averages for all four approaches in Figure 7. Results from all compilations or automated approaches display the same overall patterns, but details differ in certain regions. Our measurements (Figure 7d) generally most resemble those obtained by Liu-Yang (Figure 7c), whereas there are more differences to the compilation of manually picked measurements (Figure 7a), as might be expected, and the automated analysis of Walpole et al. (2014) (Figure 7b). The most significant differences from the manual splitting compilation are in the mid United States, where the compilation includes a relatively low number of measurements, whereas the agreement is better on both coasts. Both fast polarization directions and delay times from the manual splitting compilation

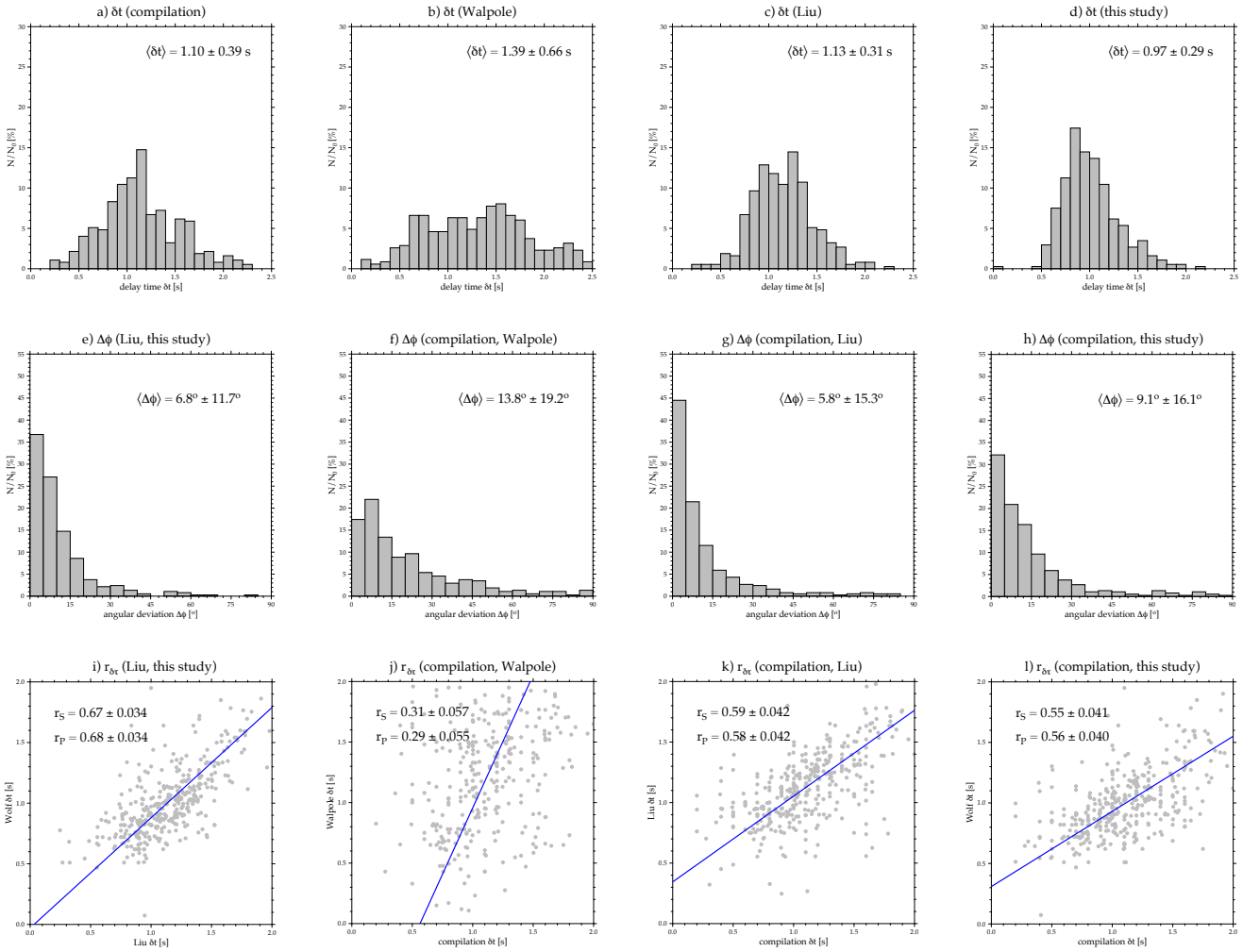

Figure 8. Statistical comparison of the binned splitting results shown in Figure 7 for North America for regions covered by the respective datasets. "Compilation" refers to the updated compilation of manual splitting studies from Becker et al. (2012), "Walpole" to the automated measurements of Walpole et al. (2014), **and** "Liu" to the automatic measurements from Liu et al. (2014) and Yang et al. (2017). (a-d) Distribution of δt values and mean values $\pm$ standard deviation for (a) the compilation of regional studies, and the automated results from (b) Walpole, (c) Liu, and (d) **this study**. (e-h) Fast polarization differences, $\Delta\phi$ and mean values between pairs of studies: **(e) Liu-this study, (f) compilation-Walpole, (g) compilation-Liu, (h) compilation-this study**. (i-l) Relationships between delay times δt between the same pairs of studies. The Pearson and Spearman rank correlations are provided as r_p and r_s with errors from bootstrapping. In general, our results are more similar to the previous automatic measurements of Liu than the compilation, but differences are larger compared to Walpole's automated estimates (not shown) which are also less similar to the compilation.

show less smooth patterns compared to the automation-based Wolf and Liu-Yang studies. The fast directions from the Walpole study roughly resemble the other approaches along the west coast of the United States, while agreement is less in the other areas.

We also conduct a statistical comparison between the measurements obtained in this study, the compilation of hand-picked measurements, and the previous Liu-Yang automated splitting measurement approach. The splitting compilation generally shows a broader spread of δt values than Liu and our study using automation-based measurements (Figure 8a, c, d), with Walpole's database showing an even wider spread (Figure 8b). The mean (expected) value of the delay time distribution are more similar for the compilation and Liu-Yang, with our estimates being $\sim 0.1 - 0.2$ s below those two for North America, and more scatter for Walpole's automated approach. Amplitude differences could potentially be explained by the broader variety of filters used to measure shear-wave splitting for these manually determined measurements. For example, for manual

measurements, higher frequencies (up to $\sim$0.5 Hz) can be used to measure δt for low splitting strength and lower frequencies (up to $\sim$0.1 Hz) for larger splitting strengths, whereas we consistently use a bandpass filter between 6 and 25 s **(see Section 3)**. This ensures consistency and comparability among measurements, but may not be ideal for any splitting strength.

We also analyze the differences in ϕ (Figure 8e-h) and δt (Figure 8i-l) across the compilation and the three automated splitting approaches. As suspected based on Figure 7, the statistical comparison shows that the results from our study are most similar to the Liu's automatic measurement approach. For both ϕ and δt, our results show a slightly greater deviation from the splitting compilation than the previous Liu-Yang automatic approach, while Walpole's estimates show larger deviations, $\sim$ twice the mean $\Delta\phi$ deviations from the compilation. Focusing on the difference between our and Liu's approach which are more comparable, those remaining more subtle differences may arise from our choice of a 6 s lower period bound of our bandpass-filter, which is generally higher (in period) than most studies in which splitting measurements are manually determined. Liu et al. (2014) and Yang et al. (2017) use a lower value of 2 s.

In general, there are multiple potential reasons for the differences between this and the previous studies that used automatic processing compared to the manual splitting compilation. First, data pre-processing varies among studies contributing to the splitting compilation. For instance, different filtering techniques are used on seismic data, and shear-wave splitting can depend on frequency (e.g., Savage, 1999; Wüstefeld et al., 2008; Wirth and Long, 2010). Second, the methods for measuring splitting may differ from the automatic approaches, which both use the transverse energy minimization technique (Silver and Chan, 1991). Other methods include the rotation-correlation method (Bowman and Ando, 1987) and the multichannel method (Chevrot, 2000). These different methods do not always produce identical results (e.g., Savage, 1999; Long and van der Hilst, 2005; Vecsey et al., 2008). Third, some studies determine the incoming backazimuth from the long-axis of the particle motion ellipse at long periods and correct the rotation of the horizontal seismogram accordingly (e.g., Liu and Gao, 2013; Wolf and Long, 2023). Others (e.g., Ekström and Busby, 2008; Reiss et al., 2019) determine an average station misorientation and adjust the splitting measurements based on that, while again others (e.g., Wolfe and Solomon, 1998) rely solely on the station misorientation provided by the data agency. These approaches vary among studies contributing to the splitting compilation. In our study, we determine the incoming backazimuth from the long-period (8-50 s) particle motion and correct the seismogram for a maximum misorientation value of 5°. If the calculated misorientation exceeds this value, no splitting parameters are determined. A systematic comparison of our individual splitting measurements with those from the splitting compilation is not possible, as many previous studies compiled in the compilation do not specify results for individual events at each station.

The Liu-Yang automatic measurements include event information for individual results, which allows us to identify the station-event pairs shared between their studies and ours. Of the 4,000 shared station-event pairs, only 15 measurements from Liu-Yang fall outside our 95% confidence intervals for either ϕ or δt. To investigate these 15 pairs in detail, we repeat splitting measurements using the same data processing as described by Liu et al. (2014). Specifically, we apply a 2-25 s bandpass-filter and do not correct for the slight backazimuthal difference determined from the long-axis of the particle motion for the individual seismogram. By adopting this approach, we generally replicate results similar to those from Liu-Yang, though minor

differences remain that could be caused a slightly different time window selection. An example of this is shown in Figure S1 of the Supplementary Material.

5.2 Global coverage

Figure 4 compares our uniformly measured dataset to the 2024 updated measurement compilation of Becker et al. (2012) which includes the database of Wüstefeld et al. (2009) updated as of 2020. The Becker compilation contains splitting measurements from restricted data that we do not have access to, for example in India, China and Saudi Arabia. Therefore, the compilation has much denser coverage in these regions. Compared to the compilation, our measurements add coverage in the central United States, northern Europe, Tajikistan, Kyrgyzstan, Australia and South America. However, this does not necessarily imply that we are the first to measure shear-wave splitting in these regions. Moreover, some existing regional studies are not part of the Wüstefeld et al. (2009) or Becker et al. (2012) compilations.

Figure 9a compares a generalized spherical harmonics expansion (cf. Becker et al., 2007) of a combination of the compilation of Becker et al. (2012) and our new automated SKS measurements with surface wave based estimates of azimuthal and radial anisotropy at asthenospheric mantle depths (175 km). As has been discussed widely, patterns of seismic anisotropy in the upper mantle are broadly consistent with convective flow in boundary layers (e.g. Tanimoto and Anderson, 1984; Montagner, 1998; Becker et al., 2008) and SKS splitting fast axes match surface wave based azimuthal anisotropy patterns on the largest scales (Montagner et al., 2000; Wüstefeld et al., 2009; Becker et al., 2012) with remaining debate about the origin of regional deviations even on scales visible on Figure 9a.

Figure 9b shows a quantitative comparison in terms of global correlation up to spherical harmonic degree $\ell = 20$, r_{20}. In this update of a similar computation shown in Becker and Lebedev (2021), the match between smoothed SKS and surface wave estimates from SL2013SVA (Schaeffer and Lebedev, 2013) and YB13SV (Yuan and Beghein, 2013) is improved slightly in the upper ~ 300 km of the mantle where we expect CPO formation under dislocation creep to dominate. The comparison with 3D2018 (Debayle et al., 2016) shows a statistically significant negative correlation at ~ 350 km. This is consistent with the comparison of Becker and Lebedev (2021) with an earlier version of the 3D2018 class of models; the physical process causing such a mismatch remain are unclear, with vertical coherence of anisotropy patterns being one possible avenue for further refinement (Yuan and Beghein, 2013).

5.3 Null stations

We compare our identified null stations to the previous work of Lynner and Long (2013) and Walpole et al. (2014). The reason to use these two studies for comparison is that they used a uniform methodology to identify stations that do not show evidence for *KS splitting. In general, our results align more closely with the study of Walpole et al. (2014): we also identify 70% of the stations they suggest as null, while this value is below 50% in the Lynner and Long (2013) study. This is likely because the dataset used by Walpole et al. (2014) is significantly larger than that of Lynner and Long (2013), and therefore more comparable to the dataset we are using.

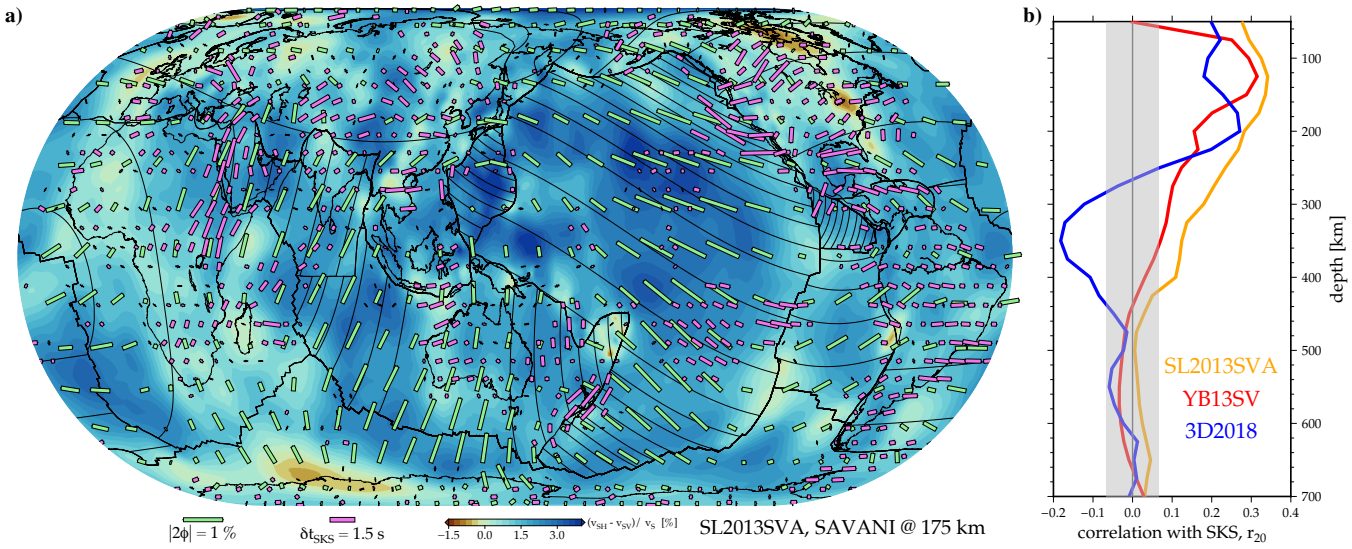

Figure 9. a) Global upper mantle anisotropy from surface wave inversions and *KS splitting. We show radial anisotropy, $\frac{v_{SH}-v_{SV}}{v_S}$, from SAVANI (Auer et al., 2014) in the background, and azimuthal anisotropy from SL2013SVA (Schaeffer and Lebedev, 2013) (green sticks) at 175 km depth, compared to a spherical harmonics fit of the station averaged SKS results (magenta sticks), up to degree $\ell = 20$ (cf. Becker et al., 2007) based on a combination of the Becker et al. (2012) compilation plus our new automated splits. Plate boundaries and absolute velocity contours from NUVEL (DeMets et al., 1994) in black lines, in the spreading-aligned reference frame of Becker et al. (2015), as an approximation of mantle shear (cf. Becker et al., 2014). **b)** Global correlation up to $\ell = 20$ between the updated SKS expansion and surface wave azimuthal anisotropy models SL2013SVA, YB13SV (Yuan and Beghein, 2013), and 3D2018 (Debayle et al., 2016). Gray region shows the range outside of which correlations can be considered significant at the 95% confidence level; figure is an update of the comparison shown in Becker and Lebedev (2021).

Once again, we focus our detailed comparison on the continental United States and southern Canada (Figure 6**b**). In this region, Walpole et al. (2014) identified numerous null stations, whereas this area was not the focus of Lynner and Long (2013). The null stations identified by Walpole et al. (2014), if not identical, are in the same general regions as those suggested in our study. Walpole et al. (2014) does not suggest null stations in the eastern United States because fewer data were available in this region at the time their study was published (Figure 7b), due to the timing of the USArray deployment.

6 DISCUSSION AND CONCLUSION

We have obtained $90,000$ $\{\phi, \delta t\}$ and $210,000$ null splitting measurements from a seismic dataset that currently contains 16 million three-component seismograms. These are six times more measurements than the largest previous uniformly measured compilation of shear-wave splitting measurements (Walpole et al., 2014). We have conducted a detailed comparison of our results with previous measurements across the United States. Our automatically determined measurements are very similar to those from Liu et al. (2014) and Yang et al. (2017), **despite the use of different codes**. Our results are also generally similar to the compilation of manual splitting results from Becker et al. (2012). However, some differences to the splitting compilation exist, which can likely be explained by the fact that the results contained in the compilation were obtained using different processing approaches, and at different seismic periods. We determine hundreds of null stations across the globe which are, in general, agreement with the previous results from Walpole et al. (2014).

There are several reasons why we believe that the data product and metadata that we are making publicly available will be a great resource for future research.

(i) The availability of both the metadata and the code package used to conduct the splitting measurements, **SplitRacerAUTO** (`https://www.geophysik.uni-frankfurt.de/64002762/Software`), ensures that all results can be reproduced. **The code version used in this study is also available at** `https://doi.org/10.5281/zenodo.14834413` **(Wolf et al., 2025).**

(ii) Our dataset includes measurements from a vast majority of openly accessible high-magnitude seismic event data. Therefore, it will give a good indication of anisotropy patterns in virtually all regions in which open-access data are available, although regional studies may be able to obtain more *KS measurements than we present in their particular study region; for example, by including lower-magnitude earthquakes.

(iii) The metadata we provide allow the inference of directional information, which is not always possible in current compilations. Therefore, our measurements can be used to determine changes in splitting parameters as a function of backazimuth, which allows detailed regional investigations (e.g., Ritter et al., 2022; Fröhlich et al., 2024).

(iv) Our measurements have been processed uniformly. For example, we used the same seismic periods for each measurement. This makes it possible to calculate sensitivity kernels as needed for anisotropic tomography approaches (e.g., Chevrot, 2006; Link and Long, 2024).

(v) We provide an extensive list of null stations, which are crucial to avoid (often unreliable) explicit anisotropy corrections in both investigations of the upper (e.g., Lynner and Long, 2013; Wolf and Long, 2023) and the lowermost mantle (e.g., Wolf et al., 2023, 2024b).

(vi) We make all diagnostic plots publicly available, implying that all measurements and automatic classifications can be individually assessed.

(vii) This dataset will be occasionally updated as more seismograms are collected as part of the massive dataset collection effort.

ACKNOWLEDGMENTS

JW was funded by the Miller Institute for Basic Research in Science at UC Berkeley. TWB, EG, KHL and JDW received support from the National Science Foundation via grants No. EAR-1927216, EAR-1855624, EAR-1853856, EAR-1853911, and EAR-1830644. The Generic Mapping Tools (Wessel and Smith, 1998) and ObsPy (Beyreuther et al., 2010) were used in this research. JW thanks Barbara Romanowicz and Weiqiang Zhu for their support, and Frederik Link for helpful discussions on **SplitRacerAUTO**. **We thank David Schlaphorst and one anonymous reviewer for constructive feedback.**

DATA AVAILABILITY

All data used in this study are publicly available and were collected and pre-processed as part of ASU's global data collection system (`http://adept.sese.asu.edu/`) for their global data products project (`http://swat.sese.asu.edu`). Data were collected from the following on-line data centers: AUSPASS (`https://auspass.edu.au/data.html`), BGR (`https://eida.bgr.de/`), CNDC (`https://www.earthquakescanada.nrcan.gc.ca/stndon/CNDC/index-en.php`),

Earthscope (http://service.iris.edu/), ETH (https://eida.ethz.ch/), FNET (https://www.fnet.bosai.go.jp/top.php?LANG=en), GEOFON (https://geofon.gfz-potsdam.de/) (GFZ Data Services, 1993), GDMS (https://gdmsn.cwb.gov.tw/) (Central Weather Bureau, 2012), ICGC (https://www.icgc.cat/en/Ciutada/Explora-Catalunya/Terratremols), INGV (http://cnt.rm.ingv.it/en/webservices_and_software), IPGP (http://ws.ipgp.fr/) (Institut de physique du globe de Paris (IPGP) and École et Observatoire des Sciences de la Terre de Strasbourg (EOST), 1982), KNMI (http://rdsa.knmi.nl/), KOERI (http://www.koeri.boun.edu.tr/new/en), LMU (http://erde.geophysik.uni-muenchen.de/), NCEDC (https://ncedc.org/) (UC Berkeley Seismological Laboratory, 2014), NIEP (https://www.infp.ro/), NOA (http://bbnet.gein.noa.gr/HL/), ORFEUS (http://www.orfeus-eu.org/), RESIF (https://seismology.resif.fr/) (RESIF, 1995), SCEDC (https://scedc.caltech.edu/) (Caltech, 2014), SSN (http://www.ssn.unam.mx/) (Instituto de Geofísica, Universidad Nacional Autónoma de México, México, 2024), TEXNET (http://rtserve.beg.utexas.edu/), and USP (https://sismo.iag.usp.br/). All networks and network citations are included as Supplementary Information, and were derived from the FDSN network code list (https://fdsn.org/networks/).

All splitting measurements are available **as text files** in the Supplementary Material. Additionally, measurements can be downloaded at http://swat.sese.asu.edu. Occasional updates will be made available on that website. **MATLAB structures with all measurements and matadata that include, for example, the selected time windows and precise event origin times are available at** https://doi.org/10.5281/zenodo.14834413 **(Wolf et al., 2025). Splitting measurements from Liu et al. (2014), Yang et al. (2017) and Walpole et al. (2014) are available in the corresponding Supplementary Materials. The latest splitting compilation update from Becker et al. (2012) can be downloaded at** https://www-udc.ig.utexas.edu/external/becker/sksdata.html**.**

CODE AVAILABILITY

SplitRacerAUTO (Link et al., 2022) is available at https://www.geophysik.uni-frankfurt.de/64002762/Software. **The code version that we used to measure splitting is also available at** https://doi.org/10.5281/zenodo.14834413 **(Wolf et al., 2025).**

References

Ando, M., Ishikawa, Y., Yamazaki, F., 1983. Shear wave polarization anisotropy in the upper mantle beneath Honshu, Japan. Journal of Geophysical Research: Solid Earth 88, 5850–5864. doi:10.1029/JB088iB07p05850.

Auer, L., Boschi, L., Becker, T.W., Nissen-Meyer, T., Giardini, D., 2014. Savani: A variable-resolution whole-mantle model of anisotropic shear-velocity variations based on multiple datasets. Journal of Geophysical Research: Solid Earth 119, 3006–3034. doi:10.1002/2013JB010773.

Becker, T.W., Conrad, C.P., Schaeffer, A.J., Lebedev, S., 2014. Origin of azimuthal seismic anisotropy in oceanic plates and mantle. Earth and Planeteray Science Letters 401, 236–250. doi:10.1016/j.epsl.2014.06.014.

Becker, T.W., Ekström, G., Boschi, L., Woodhouse, J., 2007. Length scales, patterns, and origin of azimuthal seismic anisotropy in the upper mantle as mapped by Rayleigh waves. Geophysical Journal International 171, 451–462.

Becker, T.W., Kellogg, J.B., Ekström, G., O'Connell, R.J., 2003. Comparison of azimuthal seismic anisotropy from surface waves and finite-strain from global mantle-circulation models. Geophysical Journal International 155, 696–714. doi:10.1046/j.1365-246X.2003.02085.x.

Becker, T.W., Kustowski, B., Ekström, G., 2008. Radial seismic anisotropy as a constraint for upper mantle rheology. Earth and Planetary Science Letters 267, 213–237. doi:10.1016/j.epsl.2007.11.038.

Becker, T.W., Lebedev, S., 2021. Dynamics of the Upper Mantle in Light of Seismic Anisotropy. American Geophysical Union (AGU). chapter 10. pp. 257–282. doi:10.1002/9781119528609.ch10.

Becker, T.W., Lebedev, S., Long, M.D., 2012. On the relationship between azimuthal anisotropy from shear wave splitting and surface wave tomography. Journal of Geophysical Research: Solid Earth 117, B01306. doi:10.1029/2011JB008705.

Becker, T.W., Schaeffer, A.J., Lebedev, S., Conrad, C.P., 2015. Toward a generalized plate motion reference frame. Geophysical Research Letters 42, 3188 – 3196. doi:10.1002/2015GL063695.

Becker, T.W., Schulte-Pelkum, V., Blackman, D.K., Kellogg, J.B., O'Connell, R.J., 2006. Mantle flow under the western United States from shear wave splitting. Earth and Planetary Science Letters 247, 235–251. doi:10.1016/j.epsl.2006.05.010.

Behn, M.D., Conrad, C.P., Silver, P.G., 2004. Detection of upper mantle flow associated with the African Superplume. Earth and Planetary Science Letters 224, 259–274. doi:10.1016/j.epsl.2004.05.026.

Bernard, R., Behr, W.M., Becker, T.W., Young, D., 2019. Relationships between olivine CPO and deformation parameters in naturally deformed rocks and implications for mantle seismic anisotropy. Geochemistry, Geophysics, Geosystems doi:10.1002/2019GC008289.

Beyreuther, M., Barsch, R., Krischer, L., Megies, T., Behr, Y., Wassermann, J., 2010. Obspy: A python toolbox for seismology. Seismological Research Letters 81, 530–533. doi:10.1111/10.1785/gssrl.81.3.530.

Bird, P., 2003. An updated digital model of plate boundaries. Geochemistry, Geophysics, Geosystems 4. doi:10.1029/2001GC000252.

Bowman, J.R., Ando, M., 1987. Shear-wave splitting in the upper-mantle wedge above the Tonga subduction zone. Geophys-

ical Journal of the Royal Astronomical Society 88, 25–41. doi:10.1111/j.1365-246X.1987.tb01367.x.

Caltech, 2014. Southern California Earthquake Center. doi:10.7909/C3WD3xH1.

Central Weather Bureau, 2012. Central Weather Bureau Seismographic Network. doi:10.7914/SN/T5.

Chevrot, S., 2000. Multichannel analysis of shear wave splitting. Journal of Geophysical Research: Solid Earth 105, 21579–21590. doi:10.1029/2000JB900199.

Chevrot, S., 2006. Finite-frequency vectorial tomography: a new method for high-resolution imaging of upper mantle anisotropy. Geophysical Journal International 165, 641–657. doi:10.1111/j.1365-246X.2006.02982.x.

Chevrot, S., van der Hilst, R.D., 2003. On the effects of a dipping axis of symmetry on shear wave splitting measurements. Geophysical Journal International 152, 497–505. doi:10.1046/j.1365-246X.2003.01865.x.

Creasy, N., Miyagi, L., Long, M.D., 2020. A Library of Elastic Tensors for Lowermost Mantle Seismic Anisotropy Studies and Comparison With Seismic Observations. Geochemistry, Geophysics, Geosystems 21, e2019GC008883. doi:10.1029/2019GC008883.

Debayle, E., Dubuffet, F., Durand, S., 2016. An automatically updated S-wave model of the upper mantle and the depth extent of azimuthal anisotropy. Geophysical Research Letters 43. doi:10.1002/2015GL067329.

DeMets, C., Gordon, R.G., Argus, D.F., Stein, S., 1994. Effect of recent revisions to the geomagnetic reversal time scale on estimates of current plate motions. Geophysical Research Letters 21, 2191–2194.

Ekström, G., Busby, R., 2008. Measurements of Seismometer Orientation at USArray Transportable Array and Backbone Stations. Seismological Research Letters 79, 554–561. doi:10.1785/gssrl.79.4.554.

Evans, M.S., Kendall, J.M., Willemann, R.J., 2006. Automated SKS splitting and upper-mantle anisotropy beneath Canadian seismic stations. Geophysical Journal International 165, 931–942. doi:10.1111/j.1365-246X.2006.02973.x.

Foley, B.J., Long, M.D., 2011. Upper and mid–mantle anisotropy beneath the Tonga slab. Geophysical Research Letters 38. doi:10.1029/2010GL046021.

Fouch, M.J., Fischer, K.M., Parmentier, E.M., Wysession, M.E., Clarke, T.J., 2000. Shear wave splitting, continental keels, and patterns of mantle flow. Journal of Geophysical Research: Solid Earth 105, 6255–6275. doi:10.1029/1999JB900372.

Fröhlich, Y., Grund, M., Ritter, J.R.R., 2024. Lateral and vertical variations of seismic anisotropy in the lithosphere–asthenosphere system underneath Central Europe from long-term splitting measurements. Geophysical Journal International 239, 112–135. doi:10.1093/gji/ggae245.

Gaboret, C., Forte, A.M., Montagner, J.P., 2003. The unique dynamics of the Pacific hemisphere mantle and its signature on seismic anisotropy. Earth and Planetary Science Letters 208, 219–233. doi:10.1016/S0012-821X(03)00037-2.

GFZ Data Services, 1993. GEOFON Data Centre: GEOFON Seismic Network. doi:10.14470/TR560404.

Hudson, T., Asplet, J., Walker, A., 2023. Automated shear-wave splitting analysis for single- and multi- layer anisotropic media. Seismica 2. doi:10.26443/seismica.v2i2.1031.

Institut de physique du globe de Paris (IPGP), École et Observatoire des Sciences de la Terre de Strasbourg (EOST), 1982. Geoscope, french global network of broad band seismic stations. doi:10.18715/GEOSCOPE.G.

Instituto de Geofísica, Universidad Nacional Autónoma de México, México, 2024. SSN: Servicio Sismológico Nacional. doi:10.21766/SSNMX/SN/MX.

IRIS Transportable Array, 2003. USArray Transportable Array. doi:10.7914/SN/TA.

Kneller, E.A., van Keken, P.E., Karato, S., Park, J., 2005. B-type olivine fabric in the mantle wedge: Insights from high-resolution non-newtonian subduction zone models. Earth and Planetary Science Letters 237, 781–797. doi:10.1016/j.epsl.2005.06.049.

Kocks, U., Tomé, C., Wenk, H., 2000. Texture and Anisotropy: Preferred Orientations in Polycrystals and Their Effect on Materials Properties. Cambridge University Press.

Kong, F., Gao, S.S., Liu, K.H., 2015. A systematic comparison of the transverse energy minimization and splitting intensity techniques for measuring shear-wave splitting parameters. Bulletin of the Seismological Society of America 105, 230–239. doi:10.1785/0120140108.

Lassak, T.M., Fouch, M.J., Hall, C.E., Kaminski, É., 2006. Seismic characterization of mantle flow in subduction systems: Can we resolve a hydrated mantle wedge? Earth and Planetary Science Letters 243, 632–649. doi:10.1016/j.epsl.2006.01.022.

Link, F., Long, M.D., 2024. SItomo – A toolbox for splitting intensity tomography and application in the Eastern Alps. Journal of Geodynamics 159, 102018. doi:10.1016/j.jog.2024.102018.

Link, F., Reiss, M.C., Rümpker, G., 2022. An automatized XKS-splitting procedure for large data sets: Extension package for SplitRacer and application to the USArray. Computers & Geosciences 158, 104961. doi:10.1016/j.cageo.2021.104961.

Liu, K., Elsheikh, A., Lemnifi, A., Purevsuren, U., Ray, M., Refayee, H., Yang, B., Yu, Y., Gao, S., 2014. A uniform database of teleseismic shear wave splitting measurements for the western and central United States. Geochemistry, Geophysics, Geosystems 15, 2075–2085. doi:10.1002/2014GC005267.

Liu, K.H., Gao, S.S., 2013. Making Reliable Shear-Wave Splitting Measurements. Bulletin of the Seismological Society of America 103, 2680–2693. doi:10.1785/0120120355.

Long, M.D., Becker, T., 2010. Mantle dynamics and seismic anisotropy. Earth and Planetary Science Letters 297, 341–354. doi:10.1016/j.epsl.2010.06.036.

Long, M.D., van der Hilst, R.D., 2005. Upper mantle anisotropy beneath japan from shear wave splitting. Physics of the Earth and Planetary Interiors 151, 206–222. doi:10.1016/j.pepi.2005.03.003.

Lynner, C., Long, M.D., 2013. Sub-slab seismic anisotropy and mantle flow beneath the Caribbean and Scotia subduction zones: Effects of slab morphology and kinematics. Earth and Planetary Science Letters 361, 367–378. doi:10.1016/j.epsl.2012.11.007.

Montagner, J.P., 1998. Where can seismic anisotropy be detected in the Earth's mantle? In boundary layers. Pure Appl. Geophys. 151, 223–256.

Montagner, J.P., Griot-Pommera, D.A., Lavé, J., 2000. How to relate body wave and surface wave anisotropy? Journal of Geophysical Research: Solid Earth 105, 19015–19027. doi:10.1029/2000JB900015.

Nicolas, A., Christensen, N.I., 1987. Formation of anisotropy in upper mantle peridotites; a review, in: Fuchs, K., Froidevaux, C. (Eds.), Composition, Structure and Dynamics of the Lithosphere-Asthenosphere system. American Geophysical Union, Washington DC. volume 16 of *Geodynamics*, pp. 111–123.

Nowacki, A., Wookey, J., Kendall, J.M., 2011. New advances in using seismic anisotropy, mineral physics and geodynamics to understand deformation in the lowermost mantle. Journal of Geodynamics 52, 205–228. doi:10.1016/j.jog.2011.04.003.

Reiss, M., Rümpker, G., 2017. SplitRacer: MATLAB Code and GUI for Semiautomated Analysis and Interpretation of Teleseismic Shear-Wave Splitting. Seismological Research Letters 88, 392 — 409. doi:10.1785/0220160191.

Reiss, M.C., Long, M.D., Creasy, N., 2019. Lowermost Mantle Anisotropy Beneath Africa From Differential SKS-SKKS Shear-Wave Splitting. Journal of Geophysical Research: Solid Earth 124, 8540–8564. doi:10.1029/2018JB017160.

RESIF, 1995. RESIF-RLBP French Broad-band network, RESIF-RAP strong motion network and other seismic stations in metropolitan France. doi:10.15778/RESIF.FR.

Ritter, J., Froehlich, Y., Alonso, Y., Grund, M., 2022. Short-scale laterally varying SK(K)S shear wave splitting at BFO, Germany – implications for the determination of anisotropic structures. Journal of Seismology , 1137 – 1156doi:10.1007/s10950-022-10112-w.

Romanowicz, B., Wenk, H.R., 2017. Anisotropy in the deep Earth. Physics of the Earth and Planetary Interiors 269, 58–90. doi:10.1016/j.pepi.2017.05.005.

Rümpker, G., Silver, P.G., 1998. Apparent shear-wave splitting parameters in the presence of vertically varying anisotropy. Geophysical Journal International 135, 790–800. doi:10.1046/j.1365-246X.1998.00660.x.

Russo, R.M., Silver, P.G., 1994. Trench-Parallel Flow Beneath the Nazca Plate from Seismic Anisotropy. Science 263, 1105–1111. doi:10.1126/science.263.5150.1105.

Savage, M.K., 1999. Seismic anisotropy and mantle deformation: What have we learned from shear wave splitting? Reviews of Geophysics 37, 65 – 106. doi:10.1016/10.1029/98RG02075.

Schaeffer, A., Lebedev, S., 2013. Global shear speed structure of the upper mantle and transition zone. Geophys. J. Int. 194, 417–449.

Silver, P.G., 1996. Seismic Anisotropy beneath the Continents: Probing the Depths of Geology. Annual Review of Earth and Planetary Sciences 24, 385 – 432. doi:10.1146/annurev.earth.24.1.385.

Silver, P.G., Chan, W.W., 1991. Shear wave splitting and subcontinental mantle deformation. Journal of Geophysical Research: Solid Earth 96, 16429–16454. doi:10.1029/91JB00899.

Silver, P.G., Savage, M.K., 1994. The Interpretation of Shear-Wave Splitting Parameters In the Presence of Two Anisotropic Layers. Geophysical Journal International 119, 949–963. doi:10.1111/j.1365-246X.1994.tb04027.x.

Tanimoto, T., Anderson, D.L., 1984. Mapping convection in the mantle. Geophysical Research Letters 11, 287–290. doi:10.1029/GL011i004p00287.

Teanby, N.A., Kendall, J.M., Van der Baan, M., 2004. Automation of shear-wave splitting measurements using cluster analy-

sis. Bulletin of the Seismological Society of America 94, 453–463. doi:10.1785/0120030123.

UC Berkeley Seismological Laboratory, 2014. Northern California Earthquake Data Center. doi:10.7932/NCEDC.

Vecsey, L., Plomerová, J., Babuška, V., 2008. Shear-wave splitting measurements — problems and solutions. Tectonophysics 462, 178–196. doi:https://doi.org/10.1016/j.tecto.2008.01.021. seismic Anisotropy and Geodynamics of the Lithosphere-Asthenosphere System.

Vinnik, L., Kosarev, G.L., Makeyeva, L.I., 1984. Anisotropy of the lithosphere from the observations of SKS and SKKS phases. Proc. Acad. Sci. USSR 278, 1335–1339.

Walpole, J., Wookey, J., Masters, G., Kendall, J.M., 2014. A uniformly processed data set of SKS shear wave splitting measurements: A global investigation of upper mantle anisotropy beneath seismic stations. Geochemistry, Geophysics, Geosystems 15, 1991–2010. doi:10.1002/2014GC005278.

Walsh, E., Arnold, R., Savage, M.K., 2013. Silver and Chan revisited. Journal of Geophysical Research: Solid Earth 118, 5500–5515. doi:10.1002/jgrb.50386.

Wessel, P., Smith, W.H.F., 1998. New, improved version of generic mapping tools released. Eos, Transactions American Geophysical Union 79, 579–579. doi:10.1029/98EO00426.

Wirth, E., Long, M.D., 2010. Frequency-dependent shear wave splitting beneath the Japan and Izu-Bonin subduction zones. Physics of the Earth and Planetary Interiors 181, 141–154. doi:10.1016/j.pepi.2010.05.006.

Wolf, J., Becker, T.W., Garnero, E., Liu, K.H., West, J.D., 2025. Additional data/codes concerning "Comprehensive global dataset of uniformly processed shear-wave splitting measurements". doi:10.5281/zenodo.14834413.

Wolf, J., Li, M., Long, M.D., Garnero, E., 2024a. Advances in mapping lowermost mantle convective flow with seismic anisotropy observations. Reviews of Geophysics 62, e2023RG000833. doi:10.1029/2023RG000833.

Wolf, J., Long, M., 2024. ScS shear-wave splitting in the lowermost mantle: Practical challenges and new global measurements. Seismica doi:10.26443/seismica.v3i1.1128.

Wolf, J., Long, M.D., 2022. Slab-driven flow at the base of the mantle beneath the northeastern Pacific Ocean. Earth and Planetary Science Letters 594, 117758. doi:10.1016/j.epsl.2022.117758.

Wolf, J., Long, M.D., 2023. Upper Mantle Anisotropy and Flow Beneath the Pacific Ocean Revealed by Differential PS-SKS Splitting. Geophysical Research Letters 50, e2023GL104402. doi:10.1029/2023GL104402.

Wolf, J., Long, M.D., Creasy, N., Garnero, E., 2023. On the measurement of Sdiff splitting caused by lowermost mantle anisotropy. Geophysical Journal International doi:10.1093/gji/ggac490.

Wolf, J., Long, M.D., Frost, D.A., 2024b. Ultralow velocity zone and deep mantle flow beneath the Himalayas linked to subducted slab. Nature Geoscience , 1–7doi:10.1038/s41561-024-01386-5.

Wolf, J., Long, M.D., Frost, D.A., Nissen-Meyer, T., 2024c. The expression of mantle seismic anisotropy in the global seismic wavefield. Geophysical Journal International 238, 346–363. doi:10.1093/gji/ggae164.

Wolf, J., Long, M.D., Leng, K., Nissen-Meyer, T., 2022. Constraining deep mantle anisotropy with shear wave splitting measurements: Challenges and new measurement strategies. Geophysical Journal International 230, 507–527. doi:10.